Eikonal gradient-enhanced regularization of anisotropic second-order tensorial continuum damage models for quasi-brittle materials

Breno Ribeiro Nogueira, Giuseppe Rastiello, Cédric Giry, Fabrice Gatuingt, Carlo Callari

Eikonal gradient-enhanced regularization of anisotropic second-order tensorial continuum damage models for quasi-brittle materials

Breno Ribeiro Nogueira[a,b,*], Giuseppe Rastiello[c,*], Cédric Giry[a], Fabrice Gatuingt[a], Carlo Callari[b]

[a] *Université Paris-Saclay, CentraleSupelec, ENS Paris-Saclay, CNRS, LMPS - Laboratoire de Mecanique Paris-Saclay, 4 avenue des sciences, Gif-sur-Yvette, 91190, France*

[b] *Universita degli Studi del Molise, DiBT, Via Francesco De Sanctis, 1, Campobasso, 86100, Italy*

[c] *Université Paris-Saclay, CEA, Service d'Etudes Mécaniques et Thermiques, Gif-sur-Yvette, 91191, France*

Abstract

Continuum damage models are often employed to represent cracking in quasi-brittle materials (*e.g.*, concrete, masonry and some rocks). However, from a numerical perspective, these models yield mesh-dependent results at the structural scale without regularization. Standard regularization techniques are prone, however, to some well-known drawbacks. To address these limitations, non-local models with evolving interactions have been proposed. Inspired by the analogy between non-local interactions and wave propagation time in a damaged domain, the eikonal non-local regularization introduces evolving non-local interactions through a damage-dependent metric field. The contribution of the paper involves coupling for the first time the gradient-enhanced version of the the eikonal non-local formulation with a second-order anisotropic damage constitutive model. Such an aspect is essential when modeling quasi-brittle materials, since the material response is anisotropic and associated with various well-established behaviors, including the dissymmetry between tension and compression and unilateral effect. The manuscript provides a detailed overview of the formulation, numerical solution methods, and test cases, demonstrating some important features of these models. Attention is focused not only on the regularization properties of the formulation but also on its capability to naturally represent the transition from damage to fracture.

Keywords: gradient-enhanced regularization, damage-dependent interactions, eikonal non-local formulation, anisotropic damage model, three-dimensional simulations

1. Introduction

Various anisotropic damage models have been developed to represent quasi-brittle materials such as concrete, masonry, and certain types of rocks. These models use different representations of damage, including vectors (Krajcinovic and Fonseka, 1981), second-order tensors, fourth-order tensors (Krajcinovic and Mastilovic, 1995; Maire and Chaboche, 1997), and even eighth-order tensors (Chaboche, 1982). However, fourth-order and eighth-order tensors prove to be too complex due to the large number of components, making them challenging to fully identify. Consequently, many authors have chosen to work with second-order tensors (Cordebois and Sidoroff, 1982; Ladeveze, 1983; Murakami, 1988; Halm and Dragon, 1998; Desmorat, 2004, 2015), which restrict the damage description to orthotropic behaviors. This assumption effectively captures

*Corresponding Authors

Email addresses: breno.ribeiro_nogueira@ens-paris-saclay.fr (Breno Ribeiro Nogueira), giuseppe.rastiello@cea.fr (Giuseppe Rastiello)

observed crack patterns in quasi-brittle materials, where cracks typically propagate either perpendicular or parallel to the loading direction.

An alternative approach to modeling anisotropic damage is presented in (Bažant and Oh, 1983; Bažant, 1984; Bažant and Gambarova, 1984; Bažant and Prat, 1988; Bažant et al., 1996). This approach describes material behavior independently on planes of various orientations (micro-planes) within a unitary sphere. Strain or stress vectors on each plane are obtained by projecting their respective macroscopic tensors based on static or kinematic constraints. For quasi-brittle materials, the strain tensor is projected onto each micro-plane, and simple constitutive laws are used to compute stress tensors at micro-planes. The macroscopic stress tensor is then obtained by integrating micro-plane contributions spherically based on the principle of virtual work.

From a numerical perspective, when applied to simulations at the structure scale, all the models cited above yield mesh-dependent results without regularization techniques. Non-local damage models, both integral (Pijaudier-Cabot and Bažant, 1987) and gradient-enhanced (Peerlings et al., 1996), have been employed to recover objective results. However, these methods fail to reproduce realistic cracking behavior due to issues like parasite damage diffusion, incorrect damage initiation, and attraction to domain boundaries (Geers et al., 1998; Simone et al., 2004; Pijaudier-Cabot et al., 2004; Krayani et al., 2009; Pijaudier-Cabot and Dufour, 2010; Giry et al., 2011; Desmorat, 2015; Rastiello et al., 2018; Ribeiro Nogueira et al., 2022). These drawbacks arise because the interactions are considered constant and isotropic in classic approaches.

To address these limitations, a new class of non-local evolving interaction models, known as transient internal length models, has been developed. Geers et al. (1998) proposed one of the earliest evolving interaction models, where the gradient parameter varied with strain but remained isotropic. Isotropic damage-dependent evolving interactions were introduced in (Poh and Sun, 2017), utilizing the micromorphic framework to derive a similar gradient-enhanced model. Giry et al. (2011) developed a stress-based evolving interactions integral model, more suitable to handle free boundaries. As stress fields are employed, the interactions become inherently anisotropic. A gradient-enhanced version of this anisotropic interactions approach was presented in (Vandoren and Simone, 2018). Negi et al. (2020) proposed an anisotropic transient-gradient approach based on (Poh and Sun, 2017), coupling the effects of damage and stress fields in the interactions. Several other evolving interaction models have been proposed in the literature (*e.g.*, Pijaudier-Cabot and Dufour (2010); Nguyen (2011); Rojas-Solano et al. (2013); Nguyen et al. (2018); Amani (2023)).

Inspired by the analogy between non-local interactions and wave propagation time in damaged media, Desmorat and Gatuingt (2007) and Desmorat et al. (2015) introduced the Eikonal Non-Local (ENL) regularization. This approach models non-local interactions that depend on the damage field, potentially incorporating anisotropy. In this method, non-local interaction distances are determined as the solution to a stationary eikonal equation with a damage-dependent metric field. Rastiello et al. (2018) presented a two-dimensional (2D) implementation of the integral ENL regularization for isotropic damage. Additionally, Thierry et al. (2020) and Ribeiro Nogueira et al. (2022) conducted studies on the regularization properties of the ENL approach in 1D settings. Marconi (2022) conducted two-dimensional computations utilizing an ENLG regularized isotropic damage model and investigated the coupling between damage and plasticity within a one-dimensional framework. Recently, Ribeiro Nogueira et al. (2024) provided a novel theoretical derivation of the gradient-enhanced version of ENL formulations and applied it to 2D isotropic damage mechanics simulations.

Classic non-local models, characterized by a constant internal length, have been employed in the context of anisotropic damage models in previous works. For example, Desmorat et al. (2007) utilized the conventional non-local integral approach alongside a second-order damage tensor constitutive relation. Kuhl et al. (2000) incorporated a classic gradient-enhanced model, based on the strain tensor, to regularize the anisotropic microplane formulation for quasi-brittle materials. Zreid and Kaliske (2014) proposed a simplified gradient-enhanced regularization of microplane models, where a scalar quantity is used in the regularization instead of the strain tensor. Additionally, Fassin et al. (2019) introduced a gradient-extended second-order anisotropic damage tensor model while maintaining the internal length isotropic and constant. Initial anisotropic non-local regularization, pertaining to materials with intrinsic anisotropy, has also been applied for modeling

composites (Wu et al., 2015; Jin and Arson, 2018; Forghani et al., 2019; Yin et al., 2020; Lu and Guo, 2022). Similar concepts have been explored in the phase-field community (Li and Maurini, 2019; Teichtmeister et al., 2017; Nagaraja et al., 2023), where the crack energy density was modified using structural tensors containing information about preferential microstructure directions.

This paper introduces a novel approach by coupling an evolving anisotropic interaction gradient-enhanced regularization (Desmorat et al., 2015; Ribeiro Nogueira et al., 2024) with an anisotropic damage constitutive behavior (Desmorat, 2015). The key concept is that anisotropic behavior in quasi-brittle materials, such as concrete, is induced by damage, while the medium is initially considered isotropic. The induced anisotropy is incorporated through the ENLG model, where non-local interactions naturally evolve from isotropic to anisotropic based on a damage-dependent Riemannian metric.

The manuscript is structured as follows. Sections 2 and 3 provide a brief overview of the general equations of Desmorat's anisotropic damage model (Desmorat, 2015) and the ENLG regularization. A visualization technique based on using ellipsoids is then introduced for representing damage and metric tensors, and to illustrate how induced anisotropic behavior naturally results in evolving anisotropic interactions. Section 4 details the numerical solution of the coupled problem. A staggered scheme is applied to solve the variational formulation at the global level, and an iterative Newton-Raphson procedure is used for constitutive law integration at the quadrature points. Finally, Section 5 offers a discussion concerning the main features of the presented formulation based on the 2D simulation of well-known experimental tests. A purely numerical test case is then developed to show the influence of anisotropic non-local interactions on damage evolution. Finally, a first three-dimensional simulation is briefly presented, followed by some conclusions to close the article.

2. Anisotropic eikonal gradient-enhanced damage formulation

The ENL formulation, as proposed by Desmorat et al. (2015), introduces a novel perspective on evolving non-local interactions. The underlying assumption is that damage induces deformation in the space within which interaction distances are computed. The interaction distances between the material points are obtained by solving a time-independent isotropic eikonal equation (a Hamilton-Jacobi stationary equation) with a damage-dependent Riemannian metric function. In this deformed space, the interaction distance between two points corresponds to the length of the shortest (geodesic) path connecting them (see Rastiello et al. (2018), for more details and illustrations).

2.1. Eikonal non-local formulation and anisotropic interactions

According to the general framework of anisotropic damage mechanics involving a second-order tensor damage variable $\mathbf{D}$, the differential problem for calculating the non-local variable $\bar{e}$ that controls damage evolution is computed as follows:

$$\bar{e} - \frac{c}{\sqrt{\det \mathbf{g}}} \nabla \cdot \left(\sqrt{\det \mathbf{g}}\, \mathbf{g}^{-1} \cdot \nabla \bar{e} \right) = e \qquad \Omega \tag{1}$$

$$\mathbf{g}^{-1} \cdot \nabla \bar{e} \cdot \boldsymbol{n} = 0 \qquad \partial\Omega \tag{2}$$

where $\mathbf{g}$ is a damage-dependent Riemannian metric tensor (it completely defines the deformation of the space where, according to the eikonal formalism, the non-local variable $\bar{e}$ lives):

$$\mathbf{g} = (\mathbf{I} - \mathbf{D})^{-1} \tag{3}$$

In these equations, e is the local counterpart of $\bar{e}$, $\mathbf{I}$ is the second-order identity tensor, Ω is the considered domain, $\boldsymbol{n}$ is the outward normal vector to its boundary $\partial\Omega$, c is a parameter homogeneous to the square of a length (introducing an initial length scale in the formulation), ∇ is the gradient operator, $\nabla\cdot$ is the divergence operator, and the symbol $\cdot$ denotes the simple contraction between tensors.

Equation (1) was derived by Desmorat et al. (2015) from the integral-type version of the ENL model by following the same procedure employed by Peerlings et al. (1996) to derive the classic Gradient-enhanced Non-Local (GNL) formulation. Recently, Ribeiro Nogueira et al. (2024) proposed a robust thermodynamics framework based on the Micromorphic Media Theory (Forest, 2009) to derive the ENL formulation. Using concepts from differential geometry, the authors independently derived (1), obtained the boundary condition (2) (a detail not covered by Desmorat et al. (2015)), characterized energy dissipation, and verified the Clausius-Duhem inequality.

Considerations of the free-energy potential and material symmetry. To derive the ENLG model based on a micromorphic media framework, Ribeiro Nogueira et al. (2024) introduced the following free-energy potential:

$$\rho\psi = \rho\psi(\boldsymbol{\varepsilon}, \mathbf{D}, \bar{e}, \tilde{\nabla}\bar{e}) = \rho\psi_0 + \rho\psi^{nl}(\bar{e}, \tilde{\nabla}\bar{e}; \mathbf{g}^{-1}) \tag{4}$$

where $\rho\psi_0$ represents a local contribution associated with a specified damage model, and $\rho\psi^{nl}(\bar{e}, \tilde{\nabla}\bar{e}; \mathbf{g}^{-1})$ is the non-local contribution:

$$\rho\psi^{nl}(\bar{e}, \tilde{\nabla}\bar{e}; \mathbf{g}^{-1}) = \frac{1}{2}h(e-\bar{e})^2 + \frac{1}{2}hc\|\tilde{\nabla}\bar{e}\|^2_{\mathbf{g}} \tag{5}$$

$$= \frac{1}{2}h(e-\bar{e})^2 + \frac{1}{2}d\bar{e}\cdot\mathbf{g}^{-1}\cdot d\bar{e} \tag{6}$$

Here, h is a parameter homogeneous to a stiffness, $\tilde{\nabla}$ denotes the gradient computed in a curved space, $\|\bullet\|_{\mathbf{g}}$ is the Riemannian norm, and $d\bar{e}$ denotes a 1-form. See the cited work for more details.

It is noteworthy that when employing the Euclidean metric, the expression $\rho\psi^{nl}(\bar{e}, \tilde{\nabla}\bar{e}; \mathbf{g}^{-1})$ simplifies to that of the conventional GNL model (Peerlings et al., 1996, 2004). Specifically, $\rho\psi^{nl}_{\mathrm{GNL}}(\bar{e}, \nabla\bar{e}) = \frac{1}{2}h(e-\bar{e})^2 + \frac{1}{2}hc\|\nabla\bar{e}\|^2 = \frac{1}{2}h(e-\bar{e})^2 + \frac{1}{2}\nabla\bar{e}\cdot\nabla\bar{e}$ (which is similar to the phase-field crack density functions). For an isotropic medium, it can be readily verified that the latter potential maintains invariance under rotations and reflections, satisfying the isotropy condition $\rho\psi^{nl}_{\mathrm{GNL}}(\bar{e}, \mathbf{Q}\star\nabla\bar{e}) = \rho\psi^{nl}_{\mathrm{GNL}}(\bar{e}, \nabla\bar{e}), \forall, \mathbf{Q} \in \mathcal{O}(3)$, where $\mathcal{O}(3)$ denotes the orthogonal group, defined as $\mathcal{O}(3) = \{\mathbf{Q} \mid \mathbf{Q}^\top\cdot\mathbf{Q} = \mathbf{I}\}$, and $\star$ denotes a general action of a group.[1] In the case of an anisotropic medium, it is expected that $\rho\psi^{nl}_{\mathrm{GNL}}(\bar{e}, \mathbf{Q}\star\nabla\bar{e}) = \rho\psi^{nl}_{\mathrm{GNL}}(\bar{e}, \nabla\bar{e})$ for all $\mathbf{Q} \in \mathcal{H} \subset \mathcal{O}(3)$, where $\mathcal{H}$ denotes a specified symmetry group of the anisotropic material. This ensures that the anisotropic free energy remains invariant under actions respecting the material symmetry.

Now, the representation theorem (Boehler, 1987) enables the representation of the free energy as an isotropic function by introducing a structural tensor, denoted as $\mathbf{M}$. This is achieved by ensuring that $\mathbf{Q}\star\mathbf{M} = \mathbf{M}$ holds for $\mathbf{Q} \in \mathcal{H} \subset \mathcal{O}(3)$. In the context of the ENLG model, this requirement holds true with considering the structural tensor equal to the inverse of the damage-dependent Riemannian metric ($\mathbf{M} = \mathbf{g}^{-1}$). Consequently, one has:

$$\rho\psi^{nl}(\bar{e}, \mathbf{Q}\star\tilde{\nabla}\bar{e}; \mathbf{Q}\star\mathbf{g}^{-1}) = \rho\psi^{nl}(\bar{e}, \tilde{\nabla}\bar{e}; \mathbf{g}^{-1}) \quad \forall\,\mathbf{Q} \in \mathcal{O}(3) \tag{7}$$

This formulation exhibits notable similarities with those developed by Teichtmeister et al. (2017). In a similar way, Reese et al. (2021) explored the use of an anisotropic damage variable as a structural tensor in the definition of free energy.

2.2. Comparison with other gradient formulations with evolving non-local interactions

The general formalism for gradient-damage models can be expressed as follows:

$$\bar{e} - \phi\nabla\cdot(\boldsymbol{\Phi}_1\cdot\nabla\bar{e}) = e \qquad \Omega \tag{8}$$

$$\boldsymbol{\Phi}_2\cdot\nabla\bar{e}\cdot\boldsymbol{n} = 0 \qquad \partial\Omega \tag{9}$$

Now, different choices for functions $(\phi, \boldsymbol{\Phi}_1, \boldsymbol{\Phi}_2)$ lead to specific models:

[1] Here, given a second order tensor $\mathbf{A}$, one has: $\mathbf{Q}\star\mathbf{A} = \mathbf{Q}\cdot\mathbf{A}\cdot\mathbf{Q}^\top$.

(*i*) GNL model by Peerlings et al. (1996):

$$\phi = c \qquad \mathbf{\Phi}_1 = \mathbf{I} \qquad \mathbf{\Phi}_2 = \mathbf{I} \tag{10}$$

(*ii*) Micromophic model by Poh and Sun (2017):

$$\phi = c \qquad \mathbf{\Phi}_1 = g(D)\mathbf{I} \qquad \mathbf{\Phi}_2 = \mathbf{I} \tag{11}$$

where $g(D)$ is is an exponentially decreasing function of an isotropic damage variable D. It is chosen such that $g(0) = 0$ and $g(D \to 1) \to R$, with $R > 0$ a small parameter accounting for residual non-local interactions. According to this formulation non-local interactions are isotropic.

(*iii*) Stress-based gradient-damage model by Vandoren and Simone (2018):

$$\phi = c \qquad \mathbf{\Phi}_1 = \mathbf{R} \cdot \mathbf{c}(\boldsymbol{\sigma}) \cdot \mathbf{R}^\top = \mathbf{R} \cdot \left(\frac{\sigma_i}{f_t} \boldsymbol{s}_i \otimes \boldsymbol{s}_i \right) \cdot \mathbf{R}^\top \qquad \mathbf{\Phi}_2 = \mathbf{\Phi}_1 \tag{12}$$

where σ_i is the i-th principal stress component, $\boldsymbol{s}_i$ is the corresponding eigenvector, f_t is the material strength, and $\mathbf{R}$ is the rotation tensor from the basis of principal stress directions to the external basis in which $\nabla \bar{e}$ is written. This approach allows modeling introduced anisotropic non-local interactions (see Vandoren and Simone (2018) for modified expressions of tensor $\mathbf{c}(\boldsymbol{\sigma})$).

(*iv*) ENLG model by Desmorat et al. (2015) and Ribeiro Nogueira et al. (2024):

$$\phi = \frac{c}{\sqrt{\det \mathbf{g}}} \qquad \mathbf{\Phi}_1 = \sqrt{\det \mathbf{g}}\, \mathbf{g}^{-1} \qquad \mathbf{\Phi}_2 = \mathbf{g}^{-1} \tag{13}$$

Some theoretical similarities and differences between these formulations were analyzed by Ribeiro Nogueira et al. (2024). Additionally, the stress-based micromorphic model by Negi et al. (2020) retains the localizing damage character from (Poh and Sun, 2017), and couples it with anisotropic interactions based on (Vandoren and Simone, 2018). It is worth noting that, despite the differences mentioned above, both Negi et al. (2020) and Vandoren and Simone (2018) employed a scalar damage variable, with no applications to anisotropic damage behavior (*e.g.,* tensorial damage or microplane) being developed.

A few comments on anisotropic damage and anisotropic interactions. Here, we distinguish between damage-induced anisotropy at the Representative Elementary Volume (REV) scale and its effects on induced anisotropic non-local interactions at the structural level:

- At the REV level, quasi-brittle materials can be considered as initially isotropic in the sense that the measured elastic properties are the same in all directions. However, during the softening phase, these properties degrade due to the emergence of micro-cracks, which typically form along preferential directions (Berthaud, 1991; Passelègue et al., 2018). Modeling techniques should account for this behavior (see, *e.g.*, Ramtani et al. (1992); Papa and Taliercio (1996); Lemaitre et al. (2000)). Recently, Loiseau et al. (2023) demonstrated based on discrete element simulations that isotropic damage models are inadequate for describing the macroscopic stress state of materials experiencing non-proportional loading. This limitation also becomes apparent in the comparison between isotropic and anisotropic damage models in the simulation of a simple non-proportional loading-unloading REV test case (see Appendix B).
- Anisotropic damage behavior in the Fracture Process Zone (FPZ) plays also a significant role at the structural scale. Recent observations from the so called "gap-test"(Nguyen et al., 2020) demonstrated the dependency of the fracture energy and the effective FPZ size on the crack-parallel stress, *i.e.,* the normal stress in the propagation direction, or "T-stress" (Bažant et al., 2022a,b). This behavior entails an increase in fracture energy at moderate crack-parallel compression, attributed to greater friction

in inclined micro-cracks. At high compression levels, it is characterized by a widening of the FPZ and a decrease in fracture energy. According to (Bažant et al., 2022a,b; Bažant and Nguyen, 2023), to capture these effects, modeling techniques should incorporate two main ingredients: a tensorial softening (anisotropic) damage law at the REV level, capable of representing oriented micro-cracks, and two (evolving) independent characteristic lengths for the direction of the damage band and the transverse direction (anisotropic non-local interactions).

The ENLG anisotropic damage model introduced in this contribution, eventually coupled to other suitable tensorial damage laws, may contain the necessary ingredients to capture the T-stress effect. It's worth noting that other approaches, such as crack-band with microplane or lattice approaches, achieve similar outcomes (Bažant et al., 2022b; Lyu et al., 2023). Additionally, various non-local models with anisotropic interactions (*e.g.,* Giry et al. (2011); Vandoren and Simone (2018); Negi et al. (2020)) account for two evolving internal lengths.

In this paper, we focus on presenting the model, its characteristics, and numerical implementation. Evaluating its capability to verify experimental size-effect and gap-tests is beyond the scope of this work and is left for future contributions.

2.3. Anisotropic non-local interactions

In contrast to gradient formulations with isotropic damage-dependent non-local interactions, the ENL formulation provide anisotropic interactions by utilizing the inverse of the metric in (13). This section conducts a qualitative analysis of damage dependent non-local interactions.

Tensor representation via ellipses (2D) and ellipsoids (3D). Given a vector $\boldsymbol{x}$ in the orthonormal basis $\{\boldsymbol{e}_i\}$ and a symmetric second order tensor $\mathbf{T}$ written in the basis $\{\boldsymbol{e}_i \otimes \boldsymbol{e}_j\}$, a homogeneous polynomial $p(\boldsymbol{x}) = \mathbf{T}(\boldsymbol{x}, \boldsymbol{x}) = \boldsymbol{x} \cdot \mathbf{T} \cdot \boldsymbol{x}$ can be associated with $\mathbf{T}$ by exploiting the fact that this latter is a bi-linear form.

Now, considering the principal basis $\{\boldsymbol{v}_i \otimes \boldsymbol{v}_i\}$ of tensor $\mathbf{T}$, such that $\mathbf{T} = T_i \boldsymbol{v}_i \otimes \boldsymbol{v}_i$ (with T_i denoting the eigenvalues of $\mathbf{T}$), and writing $\boldsymbol{x}$ in the basis $\{\boldsymbol{v}_i\}$, the homogeneous polynomial $p(\boldsymbol{x})$ reads:

$$p(\boldsymbol{x}) = \boldsymbol{x} \cdot \mathbf{T} \cdot \boldsymbol{x} = T_i x_i^2 = \begin{cases} T_1 x_1^2 + T_2 x_2^2 & (\mathbf{T} \in \mathbb{R}^2 \times \mathbb{R}^2) \\ T_1 x_1^2 + T_2 x_2^2 + T_3 x_3^2 & (\mathbf{T} \in \mathbb{R}^3 \times \mathbb{R}^3) \end{cases} \tag{14}$$

where Einstein summation was used. It is straightforward to observe that equation:

$$p(\boldsymbol{x}) = 1 \tag{15}$$

corresponds to the equation of a parametric ellipsoid in $\mathbb{R}^3$ and an ellipse in $\mathbb{R}^2$. Therefore, one can directly visualize $\mathbf{T}$ once its principal basis is known by simply plotting function (15).[2]

To obtain a better visualization of $\mathbf{T}$, one can also plot:

$$p(\boldsymbol{x}) = \boldsymbol{x} \cdot \mathbf{T}^{-2} \cdot \boldsymbol{x} = T_i^{-2} x_i^2 = \begin{cases} \dfrac{x_1^2}{T_1^2} + \dfrac{x_2^2}{T_2^2} & (\mathbf{T} \in \mathbb{R}^2 \times \mathbb{R}^2) \\ \dfrac{x_1^2}{T_1^2} + \dfrac{x_2^2}{T_2^2} + \dfrac{x_3^2}{T_3^2} & (\mathbf{T} \in \mathbb{R}^3 \times \mathbb{R}^3) \end{cases} = 1 \tag{16}$$

As the inverse and the square of a symmetric tensor are both isomorphisms (structure-preserving bijections), the above polynomial preserves all the properties of (15).

[2]This visualization technique is often employed for representing the stress tensor (via the Lamé's stress ellipsoids), Reynolds stress anisotropy (Hamilton and Cal, 2015) or in diffusion-tensor imaging (Westin et al., 2002).

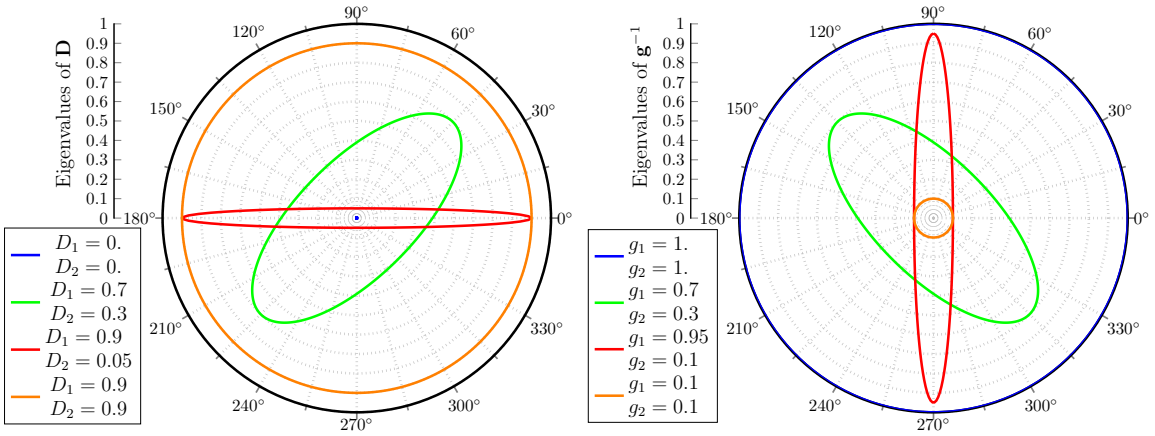

Figure 1: Ellipse representation of tensors $\mathbf{D}$ and $\mathbf{g}^{-1}$.

Damage and metric tensors representations in 2D. Consider the general form of the two-dimensional damage tensor $\mathbf{D}$ and the corresponding metric inverse $\mathbf{g}^{-1}$ (written in their principal basis):

$$\mathbf{D} = D_1 \boldsymbol{v}_1 \otimes \boldsymbol{v}_1 + D_2 \boldsymbol{v}_2 \otimes \boldsymbol{v}_2 \qquad \mathbf{g}^{-1} = (1 - D_1)\boldsymbol{v}_1 \otimes \boldsymbol{v}_1 + (1 - D_2)\boldsymbol{v}_2 \otimes \boldsymbol{v}_2 \tag{17}$$

Figure 1 shows their polar visualizations using ellipses in $\mathbb{R}^2$ (oriented according to the principal basis). Four different cases are considered to illustrate the influence of the anisotropic damage (figure 1 left) on $\mathbf{g}^{-1}$ (figure 1 right) (which can be seen as a non-local interactions tensor):

- In the undamaged state, the damage tensor $\mathbf{D} = \mathbf{0}$ is represented by a single point located at the origin of the axis, whereas $\mathbf{g}^{-1} = \mathbf{I}$ is represented by a circle. This corresponds to considering isotropic non-local interactions, reducing the ENLG model to the GNL model (Peerlings et al., 1996).
- If isotropic damage takes place ($D_1 = D_2 = D = 0.9$), the interaction tensor is equally reduced in all directions (orange circle in Figure 1 right).
- Anisotropic interactions are modeled when damage-induced anisotropy appears. The green curve corresponds to $D_1 = 0.7$ and $D_2 = 0.3$ with $\boldsymbol{v}_1 = \sqrt{2}/2(\boldsymbol{e}_x + \boldsymbol{e}_y)$ and $\boldsymbol{v}_2 = \sqrt{2}/2(-\boldsymbol{e}_x + \boldsymbol{e}_y)$. Since the largest damage value occurs at 45°, non-local interactions are strongly reduced in this direction.
- The red curve corresponds to the almost uni-axial damage case in the direction of the axis x, *i.e.*, $D_1 = 0.9$ and $D_2 = 0.05$ with $\boldsymbol{v}_1 = \boldsymbol{e}_x$ and $\boldsymbol{v}_2 = \boldsymbol{e}_y$. Therefore, the ellipse representing non-local interactions is stretched further in the vertical direction, meaning that almost no non-local interactions occur in the horizontal direction.

Damage and metric tensors representations in 3D. The same considerations hold for the three-dimensional case. Figure 2 shows the ellipsoid visualization of tensor $\mathbf{g}^{-1}$ for various uni-axial damaged states. Here, damage is considered to occur only in x direction:

$$\mathbf{D} = D_1 \boldsymbol{v}_1 \otimes \boldsymbol{v}_1 = D_{xx} \boldsymbol{e}_x \otimes \boldsymbol{e}_x \qquad \mathbf{g}^{-1} = (1 - D_{xx})\boldsymbol{e}_x \otimes \boldsymbol{e}_x \tag{18}$$

As expected, in the undamaged case, interactions are represented by a sphere. When damage occurs in the x direction, non-local interactions are progressively reduced in this direction. The higher the damage level, the more important the shrinkage of the ellipsoid in the corresponding direction.

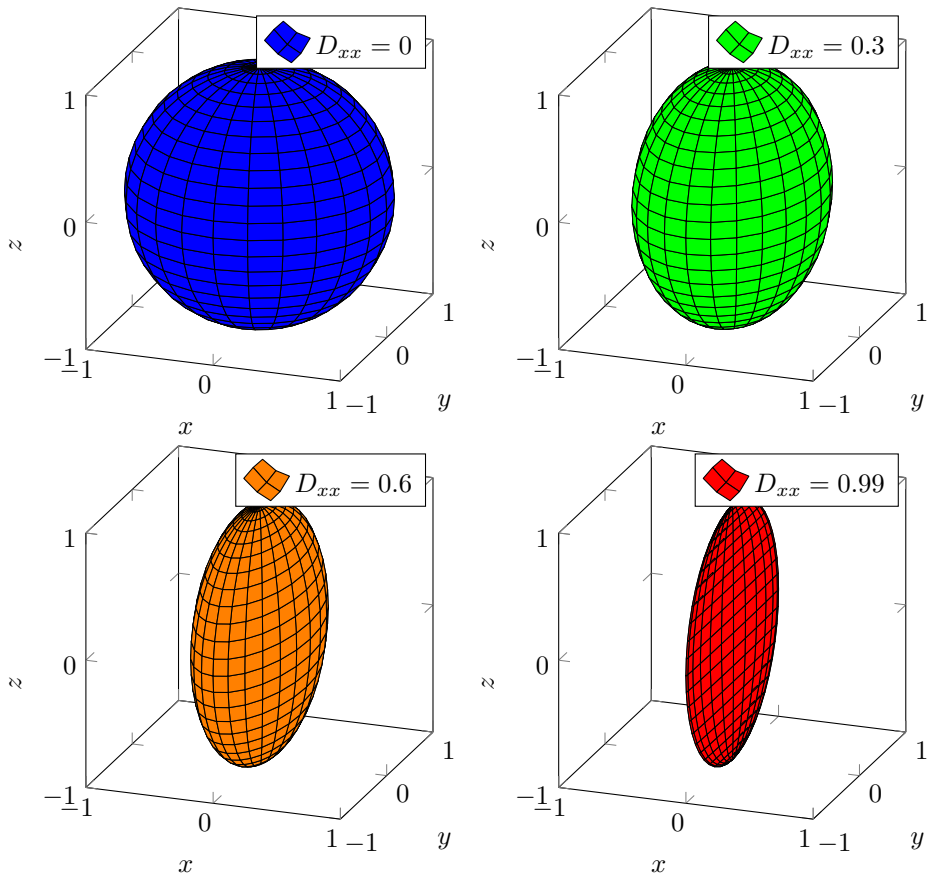

Figure 2: Ellipsoid representation of tensor $\mathbf{g}^{-1}$ for various damaged states on x direction.

2.4. Quasi-static ENLG damage mechanics boundary value problem

Let us consider a split of $\partial\Omega$ into two sub-domains $\partial\Omega_t$ and $\partial\Omega_u$ such that $\partial\Omega_u \cup \partial\Omega_t = \partial\Omega$ and that $\partial\Omega_u \cap \partial\Omega_t = 0$. Dirichlet boundary conditions ($\boldsymbol{u} = \boldsymbol{u}^d$) are imposed on $\partial\Omega_u$ whereas stress tractions ($\boldsymbol{\sigma} \cdot \boldsymbol{n} = \mathbf{t}^d$) are imposed on $\partial\Omega_t$. Moreover, let us introduce the following admissibility spaces:

$$\mathcal{U} = \{\boldsymbol{w} \;\; | \;\; \boldsymbol{w} \in H^1(\Omega) \;\; , \;\; \boldsymbol{w} = \boldsymbol{u}^d \;\; \text{on}\, \partial\Omega_u\} \tag{19}$$

$$\mathcal{U}(\mathbf{0}) = \{\boldsymbol{w} \;\; | \;\; \boldsymbol{w} \in H^1(\Omega) \;\; , \;\; \boldsymbol{w} = \mathbf{0} \;\; \text{on}\, \partial\Omega_u\} \tag{20}$$

$$\mathcal{V} = \{w \;\; | \;\; w \in H^1(\Omega^h)\} \tag{21}$$

where H^1 denotes a square integrable Sobolev space.

It is straightforward to demonstrate (Ribeiro Nogueira et al., 2024) that, under quasi-static conditions, the variational augmented equilibrium problem to be solved at any time t for finding a solution of the ENLG damage mechanics problem involves seeking an admissible displacement field $\boldsymbol{u} \in \mathcal{U}$ and an admissible non-local equivalent strain field $\bar{e} \in \mathcal{V}$ satisfying:

$$\int_\Omega \boldsymbol{\sigma}(\boldsymbol{u}) : \boldsymbol{\varepsilon}(\boldsymbol{v})\, dV = \int_{\partial\Omega_t} \boldsymbol{t}^d \cdot \boldsymbol{v}\, dS \;\; \forall\, \boldsymbol{v} \in \mathcal{U}(\mathbf{0}) \tag{22}$$

$$\int_\Omega \sqrt{\det\mathbf{g}}\, \bar{e}\eta\, dV + \int_\Omega c\sqrt{\det\mathbf{g}}\, (\mathbf{g}^{-1} \cdot \nabla\bar{e}) \cdot \nabla\eta\, dV = \int_\Omega \sqrt{\det\mathbf{g}}\, e\eta\, dV \;\; \forall\, \eta \in \mathcal{V} \tag{23}$$

where $\boldsymbol{\sigma}$ is the Cauchy stress tensor, $\boldsymbol{\varepsilon}$ is the small-strain tensor, $\boldsymbol{v}$ is the virtual displacement field, and η is the virtual non-local strain field.

The coupling between the two equations arises from the dependence of $\boldsymbol{\sigma}$ and $\mathbf{g}$ on the non-local strain via the damage tensor ($\bar{e}$ governs its evolution), and the dependency of e on the displacement via the selected equivalent strain definition:

$$\boldsymbol{\sigma} = \boldsymbol{\sigma}(\boldsymbol{u}, \mathbf{D}(\bar{e})) \qquad \mathbf{g} = \mathbf{g}(\mathbf{D}(\bar{e})) \qquad e = e(\boldsymbol{\varepsilon}(\boldsymbol{u})) \tag{24}$$

3. Anisotropic damage model

For illustrative purposes, this work adopts the constitutive model proposed by Desmorat (2015) for quasi-brittle materials. Different second-order damage models can be employed with the ENLG regularization, without necessitating modifications to its theoretical or numerical framework.

According to the chosen model, damage is represented using the second-order Ladevèze tensor $\mathbf{H} = (\mathbf{I} - \mathbf{D})^{-\frac{1}{2}}$. Denoting once again with $\boldsymbol{v}_i$ the eigenvectors of $\mathbf{D}$ and with D_i the corresponding eigenvalues, the Ladevèze tensor reads $\mathbf{H} = H_i \boldsymbol{v}_i \otimes \boldsymbol{v}_i = (1 - D_i)^{-\frac{1}{2}} \boldsymbol{v}_i \otimes \boldsymbol{v}_i$. As a consequence, $H_i = 1$ when $D_i = 0$ (undamaged state), and $H_i \to \infty$ when $D_i \to 1$ (fully damaged state). The unbounded nature of H_i enhances the formulation's ability to model the extreme scenario of fully damaged material at infinite strain (Desmorat, 2015). Moreover, from a numerical perspective, the unboundedness simplifies the handling of upper bounds (see, *e.g.*, Desmorat et al. (2007)) for damage tensors when implementing the constitutive law at the integration point level.

3.1. Three-dimensional constitutive model

Gibbs free enthalpy. The Gibbs free enthalpy reads:

$$\rho\psi_0^* = \rho\psi_0^*(\boldsymbol{\sigma}, \mathbf{H}) = \frac{\operatorname{tr}(\mathbf{H} \cdot \boldsymbol{\sigma}' \cdot \mathbf{H} \cdot \boldsymbol{\sigma}')}{4G} + \frac{1}{18K}\left[\frac{1}{3}\operatorname{tr}\mathbf{H}^2 \langle \operatorname{tr}\boldsymbol{\sigma}\rangle^2 + \langle -\operatorname{tr}\boldsymbol{\sigma}\rangle^2\right] \tag{25}$$

where $\langle\cdot\rangle$ denotes the Macaulay operator, $\bullet' = \bullet - \frac{1}{3}\operatorname{tr}(\bullet)\mathbf{I}$ denotes the deviatoric part of tensor $\bullet$ and, G and K are the shear and bulk modulus, respectively.

Constitutive relations. The strain tensor is obtained as:

$$\boldsymbol{\varepsilon} = \rho\frac{\partial\psi_0^*}{\partial\boldsymbol{\sigma}} = \frac{1}{2G}(\mathbf{H} \cdot \boldsymbol{\sigma}' \cdot \mathbf{H})' + \frac{1}{9K}\left[\frac{1}{3}\operatorname{tr}\mathbf{H}^2 \langle \operatorname{tr}\boldsymbol{\sigma}\rangle + \langle -\operatorname{tr}\boldsymbol{\sigma}\rangle\right]\mathbf{I} \tag{26}$$

The stress-strain constitutive relation is given by:

$$\boldsymbol{\sigma} = \tilde{\mathbb{E}} : \boldsymbol{\varepsilon} \tag{27}$$

where $\tilde{\mathbb{E}}$ represents the effective (damaged) Hooke's tensor, defined as:[3]

$$\tilde{\mathbb{E}} = 2G\left[\mathbf{H}^{-1}\,\underline{\overline{\otimes}}\,\mathbf{H}^{-1} - \frac{\mathbf{H}^{-2}\otimes\mathbf{H}^{-2}}{\operatorname{tr}\mathbf{H}^{-2}}\right] + m(\mathbf{H})\mathbf{I}\otimes\mathbf{I} \qquad m(\mathbf{H}) = \begin{cases} \frac{3K}{\operatorname{tr}\mathbf{H}^2} & \text{if } \operatorname{tr}\boldsymbol{\varepsilon} > 0 \\ K & \text{otherwise} \end{cases} \tag{29}$$

Here, $\otimes$ denotes the tensor product[4] and $\underline{\overline{\otimes}}$ is the symmetrized tensor product.[5]

[3] For an undamaged medium, $\mathbf{H} = \mathbf{I}$ and the undamaged Hooke's tensor is retrieved. With $\lambda = K - 2G/3$ being the Lamé's parameter, one has:

$$\tilde{\mathbb{E}} = \mathbb{E} = 2G\left[\mathbf{I}\,\underline{\overline{\otimes}}\,\mathbf{I} - \frac{\mathbf{I}\otimes\mathbf{I}}{\operatorname{tr}\mathbf{I}}\right] + \frac{3K}{\operatorname{tr}\mathbf{I}}\mathbf{I}\otimes\mathbf{I} = 2G\,\mathbf{I}\,\underline{\overline{\otimes}}\,\mathbf{I} + \lambda\,\mathbf{I}\otimes\mathbf{I} \tag{28}$$

[4] Given three vectors $\boldsymbol{a}$, $\boldsymbol{b}$ and $\boldsymbol{c}$, the tensor product is defined as $(\boldsymbol{a}\otimes\boldsymbol{b})\cdot\boldsymbol{c} = (\boldsymbol{a}\cdot\boldsymbol{c})\boldsymbol{b}$.

[5] Given three second order tensors $\mathbf{A}$, $\mathbf{B}$ and $\mathbf{C}$, the symetrized tensor product is defined as $(\mathbf{A}\,\underline{\overline{\otimes}}\,\mathbf{B}) : \mathbf{C} = \mathbf{A}\cdot\mathbf{C}\cdot\mathbf{B}$. Here, symbol : denotes the double contraction between tensors; given two second order tensors $\mathbf{A}$ and $\mathbf{B}$, one has, $\mathbf{A} : \mathbf{B} = A_{ij}B_{ij}$.

Damage criterion function. The local damage criterion function reads:

$$f = e - \kappa \tag{30}$$

where e is an equivalent measure of the strain (computed using, *e.g.*, the Mazars (1984) or Von Mises definitions), and κ is the consolidation function:

$$\kappa = \kappa_0 + SR_v^s(\operatorname{tr}\mathbf{H} - 3) \tag{31}$$

In non-local computations, the damage criterion function (30) is simply modified by substituting e with $\bar{e}$.

Here, S, s and κ_0 are material parameters, and R_v is the triaxiality function (Lemaitre, 1996). According to Desmorat (2015), this latter function is computed as:

$$R_v = \min\left[1 + \frac{9}{2}\frac{1-2\nu}{1+\nu}\left\langle -T_X\right\rangle^2, B\right] \qquad T_X = \sigma_H/\sigma_{eq} \tag{32}$$

where σ_{eq} is the Von Mises equivalent stress and $\sigma_H = \operatorname{tr}\boldsymbol{\sigma}/3$ is the hydrostatic stress. Moreover, ν stands for Poisson's ratio and B is a new material parameter bounding the triaxility function in bi-compression.

Damage evolution. In the original model by Desmorat (2015), the direction of damage evolution is controlled by the effective strain tensor $\langle\tilde{\boldsymbol{\varepsilon}}\rangle = \langle\mathbb{E}^{-1} : \boldsymbol{\sigma}\rangle$. The choice of using $\langle\tilde{\boldsymbol{\varepsilon}}\rangle$ as the damaging direction was initially introduced by Chambart (2009) to avoid numerical instabilities at high strain levels. In the present work, the positive part of the total strain tensor is employed. Using the normalized form proposed in (Loiseau, 2023; Masseron et al., 2023), one can write:

$$\dot{\mathbf{H}} = \dot{\lambda}\mathbf{P} \qquad \mathbf{P} = \frac{\langle\boldsymbol{\varepsilon}\rangle}{\|\langle\boldsymbol{\varepsilon}\rangle\|} \tag{33}$$

where $\mathbf{P}$ is the normalized damage direction tensor and $\dot{\lambda}$ is the damage multiplier respecting the usual Karush–Kuhn–Tucker (KKT) loading-unloading conditions.

According to Leroux (2012), such a choice allows better representing experimental crack paths. As a counterpart of this, a bifurcation can be obtained in the behavior when this choice is made. It should be noticed that is not a strong limit of the present implementation since instabilities were never experienced in numerical simulations.

3.2. Plane-stress conditions

In addition to the 3D conditions, the simulations in Section 5 will assume plane-stress conditions. The plane-stress formulation is derived using the same approach as applied by Jirásek and Suárez (2016) to the anisotropic damage model proposed by Desmorat et al. (2007).

Constitutive relations. The stress tensor is written as the sum of an in-plane (x, y) and out-of-plane (z) contribution as:

$$\boldsymbol{\sigma} = \boldsymbol{\sigma}_{\mathbf{2}} + \mathbf{e}_{\mathbf{2}}\varepsilon_z \qquad \boldsymbol{\sigma}_{\mathbf{2}} = \tilde{\mathbb{E}}_{\mathbf{2}} : \boldsymbol{\varepsilon}_{\mathbf{2}} \tag{34}$$

where:

$$\tilde{\mathbb{E}}_{\mathbf{2}} = 2G\left[\mathbf{H}_{\mathbf{2}}^{-1}\,\overline{\otimes}\,\mathbf{H}_{\mathbf{2}}^{-1} - \frac{\mathbf{H}_{\mathbf{2}}^{-2}\otimes\mathbf{H}_{\mathbf{2}}^{-2}}{\operatorname{tr}\mathbf{H}_{\mathbf{2}}^{-2} + H_z^{-2}}\right] + \tilde{K}\mathbf{I}_{\mathbf{2}}\otimes\mathbf{I}_{\mathbf{2}} \qquad \tilde{K} = \begin{cases} \frac{3K}{\operatorname{tr}\mathbf{H}^2 + H_z^2} & \text{if } \operatorname{tr}\boldsymbol{\varepsilon} > 0 \\ K & \text{otherwise} \end{cases} \tag{35}$$

$$\mathbf{e}_{\mathbf{2}} = \tilde{K}\mathbf{I}_{\mathbf{2}} - \frac{2G\mathbf{H}_{\mathbf{2}}^{-2}H_z^{-2}}{\operatorname{tr}\mathbf{H}_{\mathbf{2}}^{-2} + H_z^{-2}} \tag{36}$$

with $(\bullet)_{\mathbf{2}}$ denoting the two-dimensional counterpart of tensor $(\bullet)$. Accordingly $\mathbf{H_2}$ and $\boldsymbol{\varepsilon_2}$ contains only the in-plane components of $\mathbf{H}$ and $\boldsymbol{\varepsilon}$, respectively. From the three-dimensional constitutive relation, the component σ_z of the stress tensor is expressed as:

$$\sigma_z = \tilde{E}\varepsilon_z + \mathbf{e_2} : \boldsymbol{\varepsilon_2} \tag{37}$$

with:

$$\tilde{E} = \frac{2GH_z^{-2}\mathrm{tr}\,\mathbf{H_2}^{-2}}{\mathrm{tr}\,\mathbf{H_2}^{-2} + H_z^{-2}} + \tilde{K} \tag{38}$$

Enforcing the plane strain condition $\sigma_z = 0$, the out-of-plane strain component reads:

$$\varepsilon_z = -\frac{\mathbf{e_2} : \boldsymbol{\varepsilon_2}}{\tilde{E}} \tag{39}$$

Substitution into (34) yields:

$$\boldsymbol{\sigma} = \tilde{\mathbb{E}}^{\star} : \boldsymbol{\varepsilon_2} \qquad \tilde{\mathbb{E}}^{\star} = \tilde{\mathbb{E}}_{\mathbf{2}} - \frac{\mathbf{e_2} \otimes \mathbf{e_2}}{\tilde{E}} \tag{40}$$

Damage evolution. Damage evolution occurs as follows:

$$\dot{\mathbf{H}}_{\mathbf{2}} = \dot{\lambda}\mathbf{P_2} \qquad \dot{H}_z = \dot{\lambda}P_z \tag{41}$$

with:

$$\mathbf{P_2} = \frac{\langle \boldsymbol{\varepsilon_2} \rangle}{\|\langle \boldsymbol{\varepsilon} \rangle\|} \qquad P_z = \frac{\langle \varepsilon_z \rangle}{\|\langle \boldsymbol{\varepsilon} \rangle\|} \tag{42}$$

4. Numerical formulation

The variational formulation for the gradient problem requires solving the weak form of the equilibrium, taking into account anisotropic damage. Given that the effective Hooke's tensor $\tilde{\mathbb{E}}$ is expressed in terms of $\mathbf{H}$ for the employed damage model, anisotropic vanishing non-local interactions are introduced in the variational formulation through the damage-dependent Riemannian metric $\mathbf{g} = (\mathbf{I} - \mathbf{D})^{-1} = \mathbf{H}^2 = \mathbf{H} \cdot \mathbf{H}$.

4.1. Space/time discretized variational formulation

A spatial finite element method is used, such as the meshed domain is denoted by Ω^h. For quasi-static analysis, a pseudo-time discretization is introduced to represent the applied load, with n denoting the step of the corresponding time t_n. An iterative staggered solution is adopted, and Picard iteration is used to solve the augmented equilibrium problem. Linear shape functions are employed for both the displacement and the non-local equivalent strain fields ($\mathbb{P}_1$ fields), while the damage, strain, and stress fields are represented by piece-wise constant functions ($\mathbb{P}_0$ fields). This choice guarantees consistency between fields during the computation of constitutive behavior and helps avoid stress oscillations (Peerlings, 1999; Simone et al., 2003a).

The solving process can be summarized as follows (all quantities without a subscript are to be understood as referring to the present pseudo-time step t_{n+1}):

(i) Given the damage tensor at the previous iteration $\mathbf{H}^{h,k}$, one finds $\boldsymbol{u}^{h,k+1} \in \mathcal{U}^h$ at iteration $k+1$ such that:[6]

$$\int_{\Omega^h} \boldsymbol{\varepsilon}(\boldsymbol{u}^{h,k+1}) : \tilde{\mathbb{E}}\left(\mathbf{H}^{h,k}\right) : \boldsymbol{\varepsilon}(\boldsymbol{v}^h)\, dV = \int_{\partial\Omega_t^h} \boldsymbol{t}^d \cdot \boldsymbol{v}^h\, dS \quad \forall\, \boldsymbol{v}^h \in \mathcal{U}^h(\mathbf{0}) \tag{43}$$

where $\mathcal{U}^h$ and $\mathcal{U}^h(\mathbf{0})$ are the discretized counterparts of the admissibiliy spaces $\mathcal{U}$ and $\mathcal{U}(\mathbf{0})$

[6] At the first iteration ($k = 0$), the non-local strain and damage fields are initiated based on the last converged solution, *i.e.*, $\bar{e}^0 = \bar{e}_n$ and $\mathbf{H}^0 = \mathbf{H}_n$.

(*ii*) The local strain field is computed based on the updated displacement field, *i.e.*:

$$e^{h,k+1} = e(\boldsymbol{\varepsilon}(\boldsymbol{u}^{h,k+1})) \tag{44}$$

In computations, the Mazars and the Von Mises strain measures are employed.[7]

(*iii*) Given e^{k+1}, one searches for $\bar{e}^{h,k+1} \in \mathcal{V}^h$ satisfying:

$$\int_{\Omega^h} \det \mathbf{H}_n^h \, \bar{e}^{h,k+1} \eta^h \, dV + \int_{\Omega^h} c \det \mathbf{H}_n^h \, \boldsymbol{h}(\bar{e}^{h,k+1}; \mathbf{H}_n^h) \cdot \nabla \eta^h \, dV = \int_{\Omega^h} \det \mathbf{H}_n^h \, e^{k+1} \eta^h \, dV \quad \forall \, w^h \in \mathcal{V}^h \tag{47}$$

where:

$$\boldsymbol{h}(\bar{e}^{h,k+1}; \mathbf{H}_n^h) = (\mathbf{H}_n^h)^{-2} \cdot \nabla \bar{e}^{h,k+1} \tag{48}$$

It is noteworthy that a key assumption made here is related to $\mathbf{H}_n^h$, which represents the Ladevèze damage variable from the previous converged step. The hypothesis posits that the damage field responsible for modifying interactions remains unchanged throughout the iterations within a time step computation. This is in agreement with Rastiello et al. (2018), where the geodesic distances are computed with the last converged damage scalar field and are then utilized to compute the non-local equivalent strain field in the subsequent step. Additionally, it has been observed that convergence problems and oscillations in the solution fields arise when considering $\mathbf{H}^{h,k}$ in equation (47).

The term $(\mathbf{H}_n^h)^{-2} \cdot \nabla \bar{e}^{h,k+1}$ primarily contributes to reducing interactions (the gradient effect). As observed by Vandoren and Simone (2018), vanishing non-local interactions can lead to numerical oscillations in the response and affect convergence rate. Following a similar idea as proposed by Poh and Sun (2017), residual non-local interactions can be eventually considered by modifying equation (48) as:

$$\boldsymbol{h}(\bar{e}^{h,k+1}; \mathbf{H}_n^h) = \left[(\mathbf{H}_n^h)^{-2} + \xi \mathbf{I}\right] \cdot \nabla \bar{e}^{h,k+1} \qquad \xi \ll 1 \tag{49}$$

This allows for the consideration of the gradient term with minimal contribution upon damage re-localization.

(*iv*) Once $\bar{e}^{k+1}$ is computed, one updates $\mathbf{H}^{h,k+1} = \mathbf{H}(\bar{e}^{h,k+1})$ and substitutes it in equation (43) to continue the iteration process. The numerical algorithm is detailed in Appendix A.

(*v*) This process is repeated until convergence with respect to an L^2-norm for both fields, given by:

$$\|\bar{e}^{h,k+1} - \bar{e}^{h,k}\|^2 = \int_{\Omega^h} (\bar{e}^{h,k+1} - \bar{e}^{h,k})^2 dV \leq \mathrm{TOL}_u \tag{50}$$

$$\|\boldsymbol{u}^{h,k+1} - \boldsymbol{u}^{h,k}\|^2 = \int_{\Omega^h} (\boldsymbol{u}^{h,k+1} - \boldsymbol{u}^{h,k})^2 dV \leq \mathrm{TOL}_e \tag{51}$$

where TOL_u and TOL_e are user-defined tolerances.

The numerical implementation of the presented formulation is developed in a in-house finite element code at CEA (Badri et al., 2021; Badri and Rastiello, 2023), which is based on the `FreeFEM++` finite element solver (Hecht, 2012).

[7] The Mazars equivalent strain (Mazars, 1984) is defined as:

$$e = \sqrt{\langle \boldsymbol{\varepsilon} \rangle : \langle \boldsymbol{\varepsilon} \rangle} \tag{45}$$

whereas the von Mises definition (De Vree et al., 1995) is:

$$e = e(\boldsymbol{\varepsilon}(\boldsymbol{u})) = \frac{k-1}{2k(1-2\nu)} I_1 + \frac{1}{2k} \sqrt{\frac{(k-1)^2}{(1-2\nu)^2} I_1^2 + \frac{12k}{(1+\nu)^2} J_2'} \tag{46}$$

where k is a parameter corresponding to the ratio of the material strength in compression to that in tension. The invariants of the strain tensor are defined as $I_1 = \mathrm{tr}\boldsymbol{\varepsilon}$ and $J_2' = \frac{1}{6}\left(3\boldsymbol{\varepsilon} : \boldsymbol{\varepsilon} - \mathrm{tr}^2\boldsymbol{\varepsilon}\right)$.

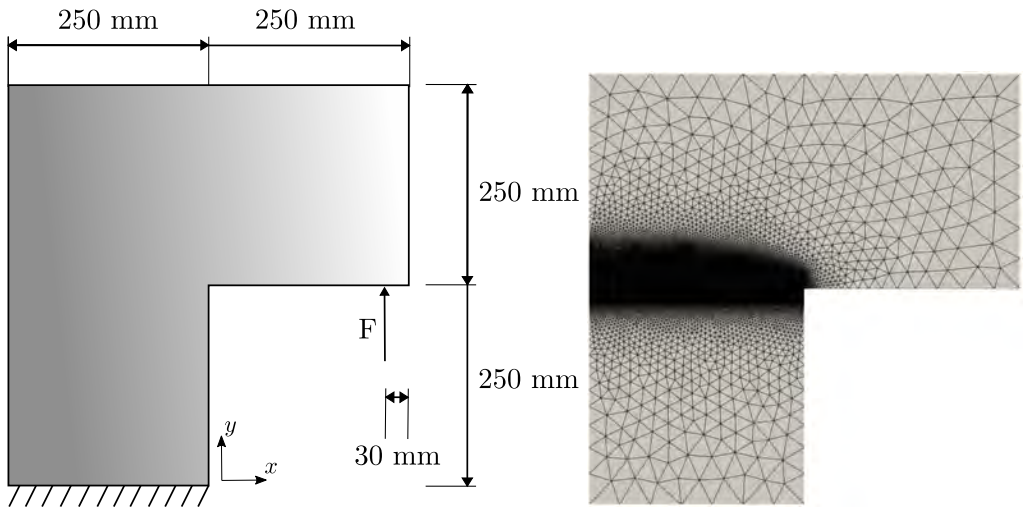

Figure 3: L-shape test – Geometry (thickness = 100 mm) and boundary conditions (Winkler et al., 2001, 2004) (left) and an example of a finite element mesh containing 205 972 CST elements (right).

Modifications to account for plane-stress conditions. As previously detailed, the decomposition of variables into out-of-plane and in-plane components is crucial. Given that $\sigma_z = 0$, the argument of the bi-linear form in equation (43) becomes:

$$\boldsymbol{\varepsilon}(\boldsymbol{u}^{h,k+1}) : \tilde{\mathbb{E}}\left(\mathbf{H}^{h,k}\right) : \boldsymbol{\varepsilon}(\boldsymbol{v}^h) = \boldsymbol{\varepsilon}_{\mathbf{2}}(\boldsymbol{u}^{h,k+1}) : \tilde{\mathbb{E}}^{\star}\left(\mathbf{H}_{\mathbf{2}}^{h,k}, H_z^{h,k}\right) : \boldsymbol{\varepsilon}_{\mathbf{2}}(\boldsymbol{v}^h) \tag{52}$$

Thus, by substituting this expression into equation (43), the weak form of equilibrium still holds. It is further assumed that $\nabla\bar{e} \cdot \mathbf{e}_z = 0$, leading to:

$$(\mathbf{H}_n^h)^{-2} \cdot \nabla\bar{e}^{h,k+1} = (\mathbf{H}_{\mathbf{2}}^h)_n^{-2} \cdot \nabla\bar{e}^{h,k+1} \tag{53}$$

Consequently, the variational equation (47) remains valid. The main distinction from the previous case is that:

$$\det \mathbf{H}_n^h = H_{n,xx}^h H_{n,yy}^h H_{n,z}^h - (H_{n,xy}^h)^2 H_{n,z}^h = H_{n,1}^h H_{n,2}^h H_{n,z}^h \tag{54}$$

4.2. Material law at integration point level

A fully implicit integration algorithm is employed for implementing the anisotropic damage model. This choice, while differing from the explicit approach utilized by Desmorat (2015), offers enhanced robustness by ensuring convergence even for larger strain increments. The implementation is carried out using the `mfront` constitutive laws generator (Helfer et al., 2015). The interface between the finite element solver and the constitutive model integrator is handled through a custom interface developed with `mgis` (Mfront Generic Interface Support). Details concerning the material law integration are discussed in Appendix A, whereas representative local responses at integration point level are addressed in Appendix B.

5. Results and discussion

Numerical 2D simulations are presented to elucidate the principal features of the proposed formulation. Initially, the simulation of the L-shape test, as conducted by Winkler et al. (2001, 2004), is carried out under plane-stress conditions. Subsequently, the focus shifts to the simulation of the three-point bending test developed by Gálvez et al. (1998). Both tests serve as a common benchmark for validating cracking models,

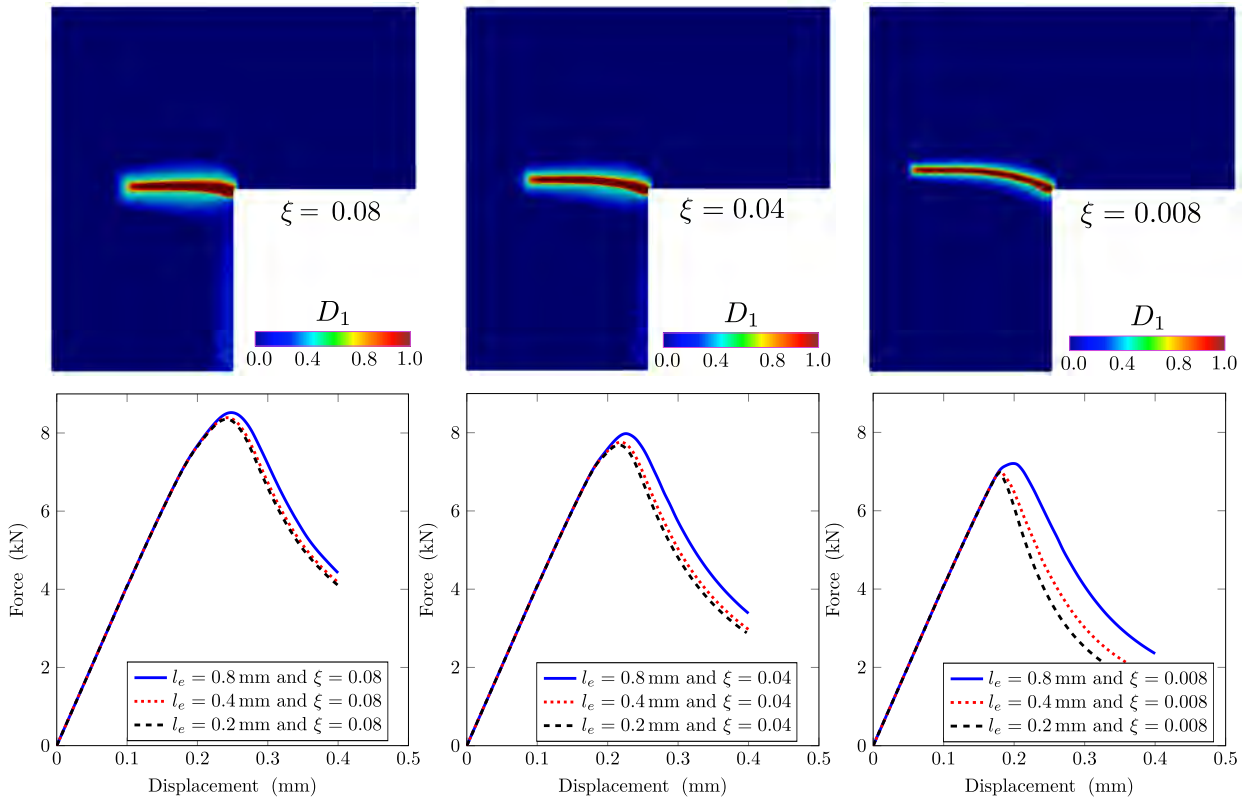

Figure 4: L-shape test – Study on the impact of ξ on the structural responses and damage maps (maximum principal damage component D_1).

especially in scenarios involving mixed-mode conditions. A novel test case simulating non-proportional loading on a hexagonal specimen is then proposed to illustrate the differences between isotropic and anisotropic damage models. Finally, a few 3D results are provided for illustrative purposes and to initiate discussion on perspectives for future developments.

5.1. Mixed-mode 2D L-shape test

Figure 3 illustrates the geometry, boundary conditions, and an example of a finite element mesh utilized. In all meshes, the characteristic element size l_e is reduced in the central part of the specimen, where, based on experimental evidence, damage is expected to occur.[8] To study mesh convergence, three different meshes are employed in the numerical simulations, containing 58 710 ($l_e = 0.8$ mm), 205 972 ($l_e = 0.4$ mm) and 753 143 ($l_e = 0.2$ mm) Constant Strain Triangles (CST), respectively. The displacement is constrained in the x and y directions at the bottom of the specimen. A displacement-controlled point load is applied vertically to represent the force denoted as F in the figure. The material is assumed to follow the anisotropic damage model described earlier, with the equivalent strain calculated using the Mazars definition (45). This decision was made to accurately predict both the peak load and the overall softening regime, following the recommendations of Nguyen et al. (2018) and as also used by Sarkar et al. (2019) for the same reasons.

Several authors (Oliver et al., 2004; Nguyen et al., 2018) have noted that the elastic material parameters provided by Winkler et al. (2001, 2004) cannot be directly applied in numerical simulations as they lead to an

[8]Finite element meshes are generated using the GMSH mesh generator. Accordingly, the characteristic element size correspond to the length of mesh edges.

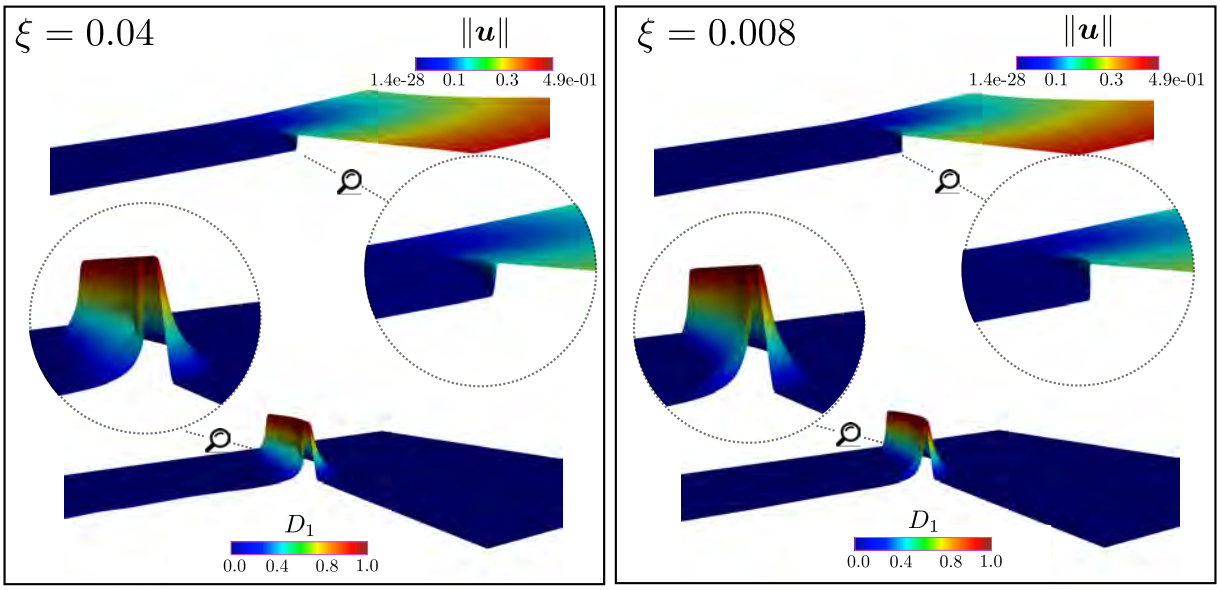

Figure 5: L-shape test – Warp by scalar plots of the first damage eigenvalue D_1 and the norm of the displacement field $\|\boldsymbol{u}\|$

overestimation of the initial structural stiffness.[9] In the following, to achieve an elastic response consistent with experimental data, Young's modulus is set to $E = 17\,000$MPa (instead of $E = 25\,850$MPa, as in experiments), while the Poisson's ratio is kept equal to the experimental value ($\nu = 0.18$). Five additional material parameters must be defined for using the anisotropic damage model detailed in Section 2. In this section, the remaining material parameters are set to $\{c, \kappa_0, S, s, B\} = \{7.32\,\text{mm}^2, 1.4 \times 10^{-4}, 3.91 \times 10^{-4}, 4.9, 5/3\}$. The analysis is carried out for three different values of ξ to examine the influence of residual non-local interactions on structural responses and damage evolution.

5.1.1. Role of residual non-local interactions on mesh-convergence and damage re-localization

Structural response and mesh convergence. Figure 4 presents the structural responses and corresponding damage maps (principal value D_1) for various residual non-local interactions parameter ξ values. Convergence in the overall response with mesh refinement is attained for $\xi = 0.08$ and $\xi = 0.04$, employing a mesh containing 753 143 elements with $l_e = 0.2, \text{mm}$ in the refined region. Similarly, a trend toward mesh convergence is observed around the peak load in simulations with $\xi = 0.008$ using the same mesh. However, differences emerge in the post-peak phase between meshes with $l_e = 0.4, \text{mm}$ and $l_e = 0.2, \text{mm}$. Furthermore, the response showcases decreased brittleness with increasing ξ values, for a given set of material parameters.

Damage evolution. The reduction in brittleness observed in the structural response for larger values of ξ can be attributed to damage diffusion (Figure 4 (top)). In the original ENLG model ($\xi = 0$), non-local interactions vanish upon damage re-localization ($D_i \to 1$). However, with appropriately chosen $\xi > 0$, moderate residual non-local interactions persist, leading to minor damage spreading around the re-localized zone. This behavior also influences the propagation direction associated with the damage band. For instance,

[9] For example, Nguyen et al. (2018) considered $E = 21\,000$MPa and applied the point load at the right of the specimen (not at 30 mm from it). Wang et al. (2023) made the same assumption concerning the point load position but retained the original material parameters. Zreid and Kaliske (2014) applied the point load at a certain distance from the extremity and considered $E = 18\,000$MPa in computations.

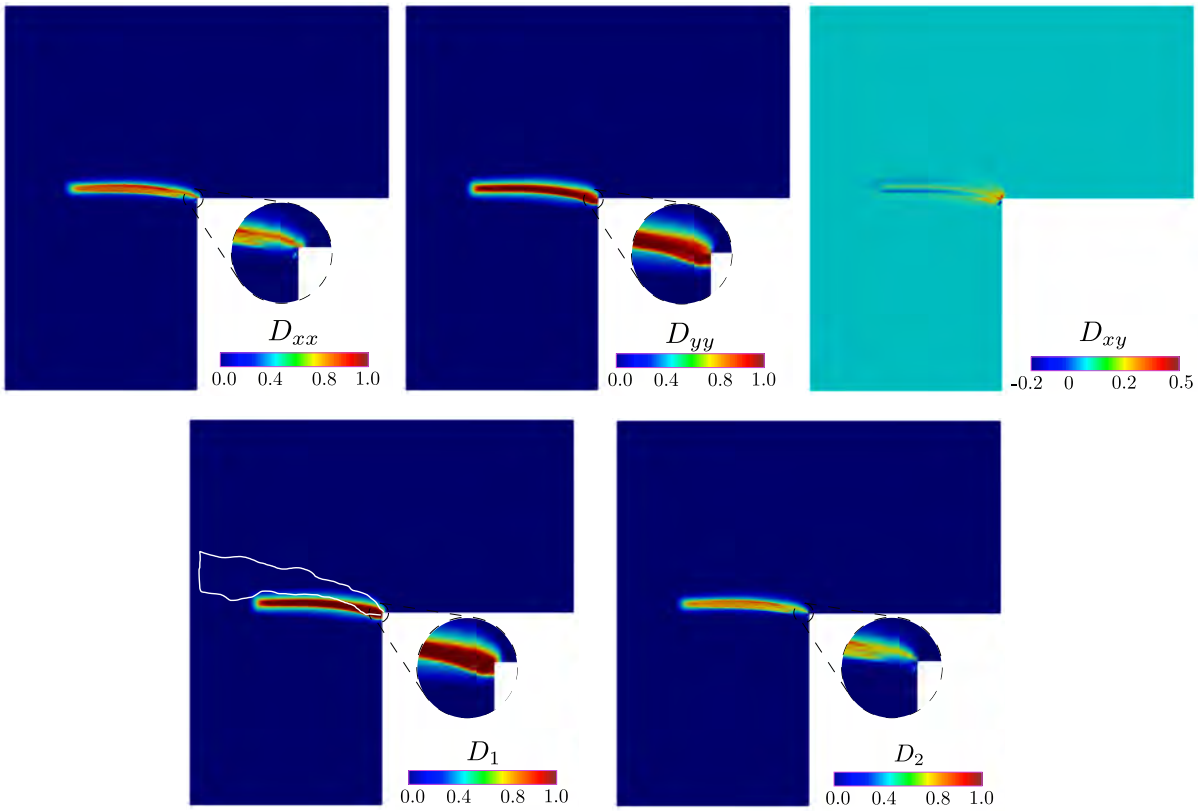

Figure 6: L-shape test – Components of the damage tensor at the end of the simulation. Solid white lines represent the envelope of experimental crack paths from Winkler et al. (2001, 2004).

the damage band is almost horizontal for $\xi = 0.08$, whereas it progressively becomes more curved as ξ decreases.

These aspects are further illustrated in Figure 5, which compares the ability of the ENLG approach to simulate the tendency toward damage-to-fracture transition for $\xi = 0.04$ and $\xi = 0.008$. The first damage eigenvalue D_1 is depicted in Figure 5 (bottom left and right), indicating damage re-localization in a narrow zone for both cases. However, the damage spreads over a larger zone for $\xi = 0.04$ compared to $\xi = 0.008$ (as shown in the zoomed-in damage maps). An approximation of a jump in the displacement field (Figure 5 (top)) is observed for both values of ξ, which corresponds, in the limit case, to the kinematics of a crack description (discontinuity). Nonetheless, the simulation better describes this approximation with $\xi = 0.008$ (as seen in the zoomed-in displacement field). It's important to note that this is merely a post-processing analysis of the results because the adopted continuous finite element formulation cannot capture displacement jumps.

On the choice of ξ. According to this analysis, the smaller the value of ξ, the better the capability of the ENLG numerical model in representing damage re-localization, thus indirectly depicting a progressive damage-to-fracture transition. As a counterpart to this, finer and finer meshes are needed to achieve mesh convergence of the structural response. The value of ξ in simulations should therefore be carefully chosen depending on the available computer resources (finer the mesh, larger are CPU times) and the intended application of the model.

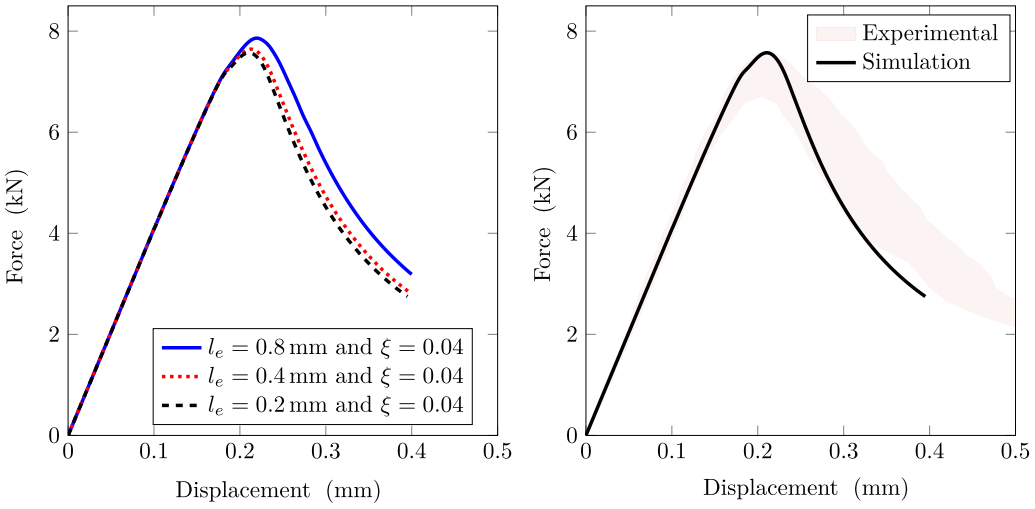

Figure 7: L-shape test – Convergence upon mesh refinement (left) and structural response obtained ($l_e = 0.2\,\text{mm}$ mesh) compared to the experimental one (Winkler et al., 2001, 2004) (right).

5.1.2. Additional analyses and comparison with experimental results

To compare the results from the numerical simulations with experimental data from the literature, we retain the value of $\xi = 0.04$ for the following analyses. This choice allows for converged results with a relatively high number of elements, yet remaining numerically feasible within a sequential solving framework[10] without excessive spreading of damage.

Representative structural response and mesh convergence. Figure 7 (right) shows the optimal (compared to experimental results) structural response obtained with $\{\kappa_0, S\} = \{1.7{\times}10^{-4}, 3.81{\times}10^{-4}\}$, while all the other parameters remain unchanged from the previous section. The overall response aligns with the experimental results, demonstrating that achieving reasonable quasi-brittle responses with the ENLG model, coupled with the presented anisotropic constitutive behavior, is feasible. Improved fitting might also be attained by modifying the damage evolution law, since the parameter S controls locally the peak and the post-peak behavior (see, *e.g.*, Loiseau (2023)).

Damage evolution. In addition to the structural responses, one can analyze the damage profiles obtained to evaluate the capability of the present approach to represent "cracking" behaviors. Figure 6 (top) shows the in-plane components (D_{xx}, D_{yy}, D_{xy}) of the damage tensor at the end of the simulation. As expected, the highest damage level is obtained in the y direction ($D_{yy} > D_{xx} > D_{xy}$), which is mainly perpendicular to the "pseudo-crack" direction. The off-diagonal component D_{xy} is more pronounced close to the corner, where damage starts. There, the principal damage directions are slightly rotated with respect to the main axes (x, y). As shown in Figure 6 (bottom), similar considerations hold when considering the principal damage components (D_1, D_2). Moreover, the envelope of crack paths obtained by Winkler et al. (2001, 2004) are represented in Figure 6 by solid white lines. One observes good agreement when comparing the damage band obtained by the ENLG model with the experimental crack paths. However, the curved cracking behavior is less present due to the choice of $\xi = 0.04$, which could be better represented for simulations with $\xi = 0.008$, as shown in Figure 4. A fitting procedure for $\xi = 0.008$ becomes prohibitive in the sequential solver framework of this contribution due to CPU time, as more elements are required to obtain a converged response.

To highlight the capabilities of the ENLG model to represent a tendency toward a transition from damage to fracture, Figure 8 displays profiles of the major principal component of the damage tensor and the

[10] Parallel solving techniques were not yet studied and are left for future work.

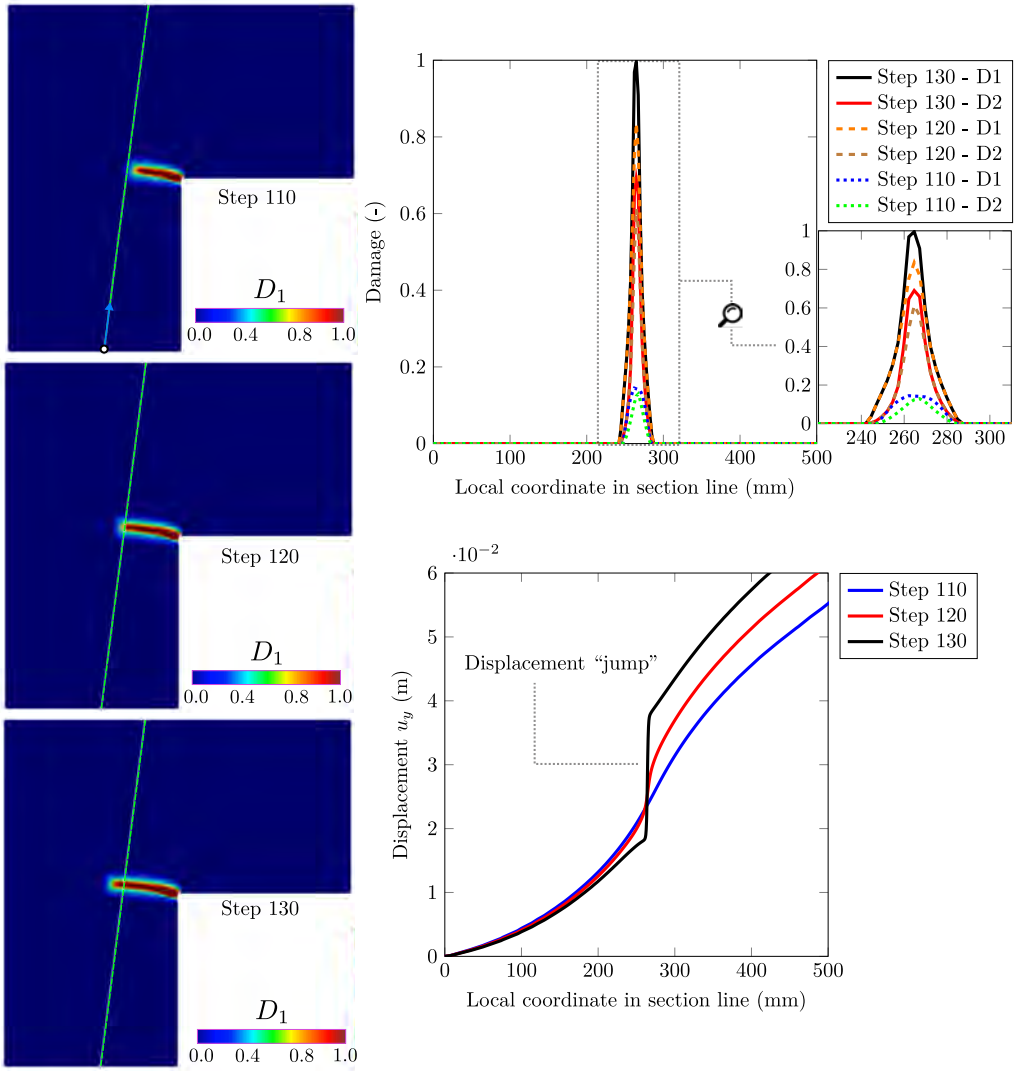

Figure 8: L-shape test – Major principal damage component and displacement magnitude along a line approximately aligned with the major principal damage direction in the center of the damaged band for three phases of the damage evolution

resulting displacement field along a line oriented approximately in the major damage principal direction. As shown in the figure, the damage field progressively increases in the region preceding the "pseudo-crack". Subsequently, the damage tends to reach a unitary value in the central zone of a band, whose maximum size remains stationary. As seen before, this is better represented for simulations where $\xi = 0.008$, but it can be still observed here ($\xi = 0.04$) at the propagation front of the damage band. At the same time, the displacement field clearly indicates a tendency toward a discontinuity centered in the middle of the damage band. It is worth noting, however, that this discontinuity cannot be represented in the formulation presented here, as the displacement field is assumed to be continuous by construction.

5.2. Mixed-mode 2D three-point bending test

The geometric details and boundary conditions for this case are illustrated in Figure 9 (top). This configuration corresponds to the small specimens examined in the referenced study, featuring a notch with a width of 2 mm. Four finite element meshes were utilized in the numerical simulations, comprising 4333,

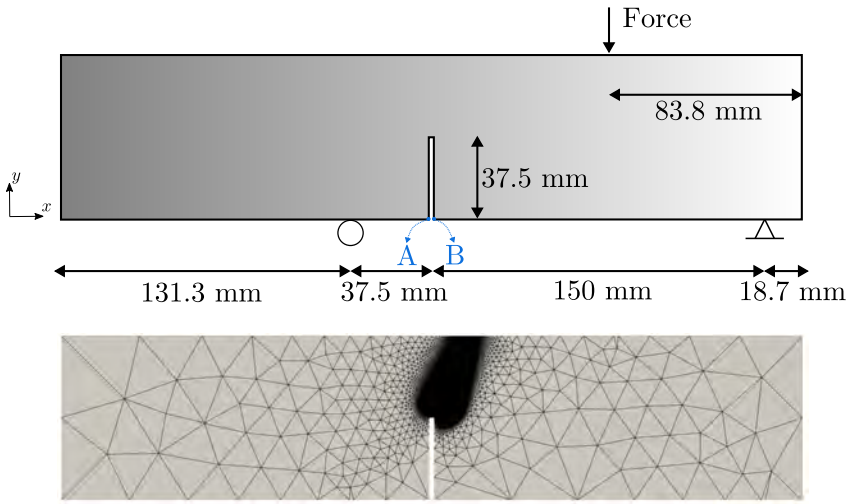

Figure 9: Three-point bending test – Geometry (thickness = 50 mm) and boundary conditions (top) and example of a mesh containing 178 476 elements (bottom).

13422, 47564, and 178476 CST elements, respectively (Figure 9 (bottom)). All meshes are locally refined around the notch tip where the onset of damage is expected to occur.. The displacement was applied at the upper part of the beam under CMOD (Crack Mouth Opening Displacement) control (calculated as the relative displacement of points A and B in figure 9).[11] The material parameters for this test are chosen as $\{E, \nu, c, \kappa_0, S, s, B\} = \{38'000\text{ MPa}, 0.2, 1.0\,\text{mm}^2, 6\times10^{-4}, 2\times10^{-4}, 4.9, 5/3\}$. Moreover, $\xi = 0.04$. Similar to the L-shape test, Mazars' equivalent strain is utilized in the computations.

5.2.1. Mesh-convergence in terms of damage maps and structural response

Figure 10 shows the damage maps (depicting the first principal damage value D_1) obtained for the different meshes alongside the corresponding structural responses. One can observe convergence of the damage pattern upon mesh refinement, as well as in terms of the structural response. Regarding the overall response, convergence is achieved with a mesh containing 178 476 elements with $l_e = 0.1$ mm in the refined region. Thus, the characteristic size of elements required to obtain convergence in this example is two times smaller than the one for the L-shape test. This can be attributed to the use of a smaller gradient parameter c used for the three-point bending test.

5.2.2. Representative results

Representative structural response and comparison to experimental results. Similar to the L-shape test, the elastic parameters provided by Gálvez et al. (1998) lead to an overestimation of the initial structural stiffness. To achieve an elastic response consistent with experimental data in this test case, the Young's modulus is set to $E = 33\,000$ MPa in the following simulations. Additionally, to ensure good agreement between simulations and experimental results, the following parameters are also modified: $\{\kappa_0, S\} = \{7\times10^{-4}, 2.4\times10^{-4}\}$. All other parameters remain the same as those used to obtain the results depicted in Figure 10.

The structural responses obtained for the different meshes are depicted in Figure 11 (left). With the new set of parameters, mesh convergence is again achieved with the mesh containing 178 476 elements (with

[11] A simple path-following algorithm is employed for this purpose, treating the magnitude of the external load as a novel unknown and enhancing the damage mechanics equilibrium problem through an additional constraint equation. A detailed description of the final algorithm is omitted here for conciseness, but further information can be found in (de Borst, 1987; Rastiello et al., 2019, 2022), among others.

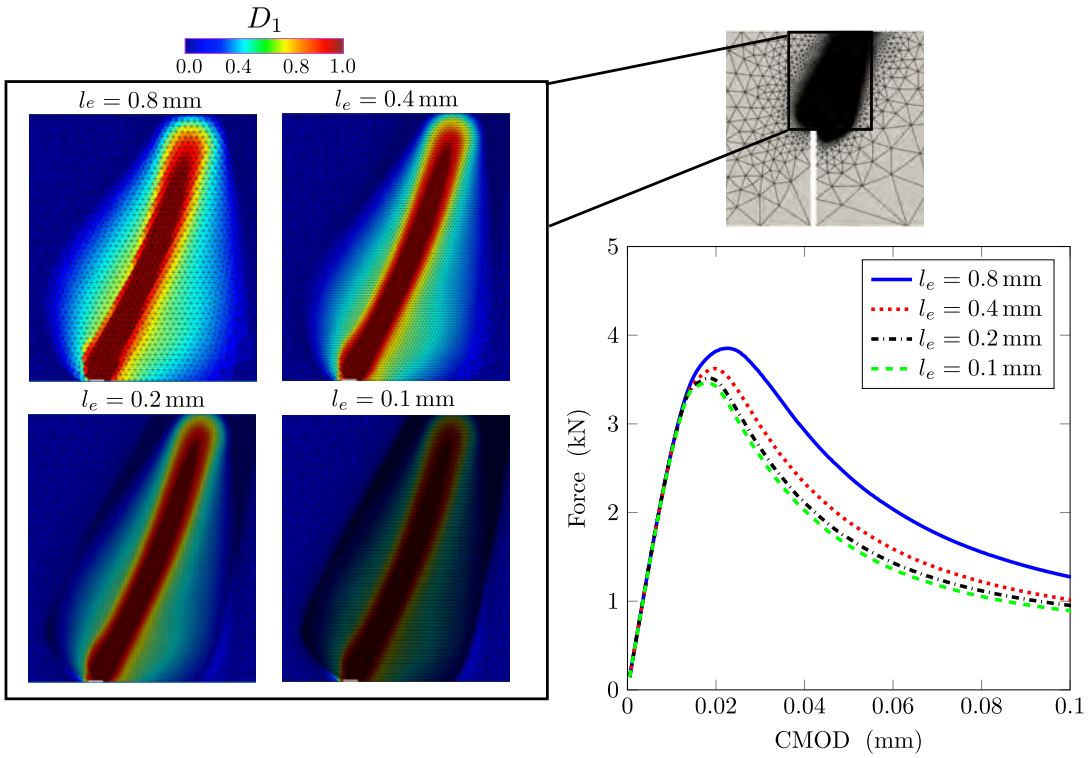

Figure 10: Three-point bending test – Mesh convergence in terms of damage maps and structural response.

$l_e = 0.1\,\text{mm}$ in the refined region). In Figure 11 (center), a comparison is presented between the experimental and numerical (converged) structural Force vs. CMOD responses. It is shown that the numerical simulation provides a good estimation of the ultimate force and effectively captures significant quasi-brittle behavior. Figure 11 (right) compares the experimental crack paths (depicted in white) with the damage pattern (D_1 in this case) obtained using the ENLG model at the simulation's conclusion. A good agreement with experimental results is evident, particularly concerning the direction of damage propagation. This underscores the ENLG regularization's ability to replicate realistic crack paths while providing reasonable quasi-brittle responses at the structural scale. However, far from the notch and near the upper part of the beam, the damage pattern tends to the left of the envelop crack paths.

Damage evolution. The evolution of the damage maps obtained using the mesh with $l_e = 0.1\,\text{mm}$ mesh for three different loading stages (CMOD $= 0.02\,\text{mm}$, $0.06\,\text{mm}$ and $0.1\,\text{mm}$) is presented in Figure 12.

Consistent with experimental observations, the damage band exhibit an orientation to the right of the notch and a slight curvature toward the top of the beam. The D_{xx} profile indicates considerable damage along the x direction, although it does not consistently align with the principal directions in all elements. Similarly, the D_{yy} profile, along with the profile for the off-diagonal term D_{xy} (central column in Figure 12), reveal that principal directions deviate from the Cartesian axes.

Similar considerations on the damage mechanisms emerge when analyzing the eigenvalues of the damage tensor. The last two columns in Figure 12 depict color maps for D_1 and D_2, obtained at the Gauss points (D_1 represents the largest damage eigenvalue). The D_1 damage map clearly illustrates the emergence of an equivalent "macro-crack" in a specific preferential direction. As anticipated, neither D_1 nor D_2 correspond precisely to the D_{xx} and D_{yy} damage maps; instead, they represent a combination of the two. This is crucial for accurately modeling the direction of crack paths and the associated principal damage perpendicular to them. The evolution of D_1 highlights also the minor spread of damage upon re-localization. It presents a

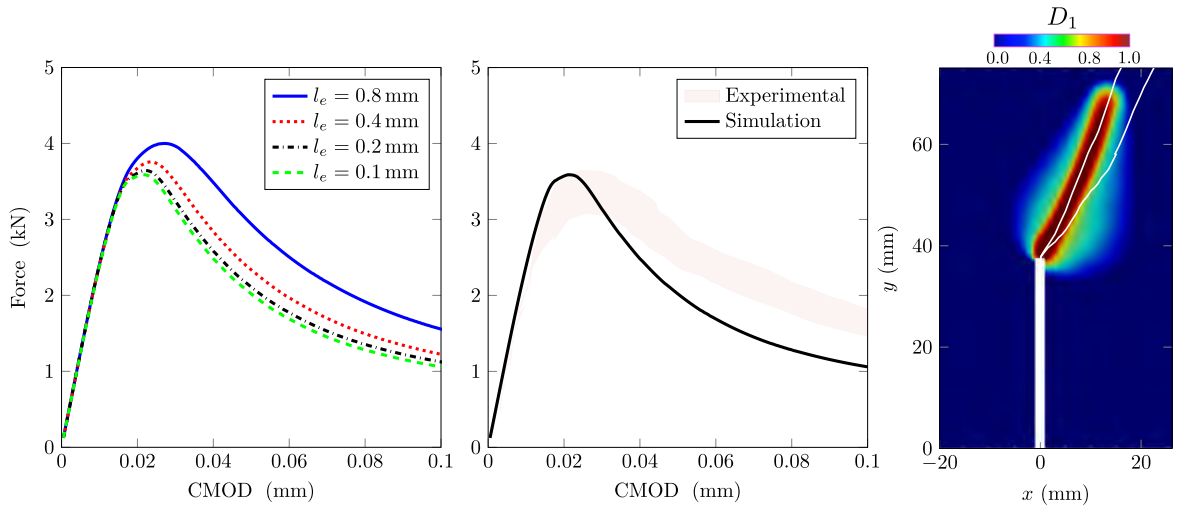

Figure 11: Three-point bending test – Convergence upon mesh refinement in terms of the overall response (left). Comparison between numerical ($l_e = 0.1\,\text{mm}$ mesh) and experimental responses (center). Comparison between experimental crack paths (white solid lines) and the damage pattern obtained at the end of the simulation (right).

sharp profile at the propagation front of the damage band and spreads damage behind it due to the residual non-local interactions.

Non-local interactions evolution. Considering the obtained results regarding principal damage orientation, it is anticipated that nonlocal interactions are significantly diminished in the direction of the major principal damage component. If ellipses are used to represent such interactions, their radius is expected to contract in the same direction. Figure 13 illustrates the evolution of interaction ellipses (*i.e.*, tensor $\mathbf{g}^{-1} = \mathbf{H}^{-2}$) for points where CMOD $= 0.02\,\text{mm}$, $0.06\,\text{mm}$ and $0.1\,\text{mm}$ in Figure 11. For the sake of visualization, the coarse mesh containing 4 333 elements was used. Blue disks denote the initial isotropic nature of interactions at the beginning of the simulation, where $\mathbf{g}^{-1} = \mathbf{I}$.

At CMOD $= 0.02\,\text{mm}$, damage initiates from the notch and reached high levels in certain elements. As depicted in Figure 13, ellipses are oriented in the direction of damage propagation and compressed perpendicular to it. Elements traversed by collapsed ellipses lose the ability to communicate with their neighbors as interactions are reduced. However, elements to the right of the highly damaged zone can still communicate with neighbors from the right and top, which are parallel to the collapsed zone. Ahead of the zone where ellipsoids are formed, blue disks indicate that elements have not yet undergone damage. Damage propagates, and the collapsed ellipses' behavior observed at CMOD $= 0.02\,\text{mm}$ also spreads to the top of the beam at CMOD $= 0.06\,\text{mm}$ and CMOD $= 0.1\,\text{mm}$.

The evolution of the interaction ellipses, as demonstrated here, reveals the interesting characteristics of the ENLG formulation when coupled with an anisotropic damage model. The ENLG model inherently accounts for two independent material characteristic lengths for the direction of the damage band and one transverse to it. In other words, the anisotropic nature of the non-local interactions allows for a natural distinction between the transverse and parallel directions to the damage band.[12]

[12] According to Bažant et al. (2022a), the nonlocal material characteristic length should vary as a function of the normal stress in the principal direction of the damage tensor in the developing damage localization band terminating in fracture. The ENLG model, coupled with an anisotropic damage model, exhibits this desired behavior.

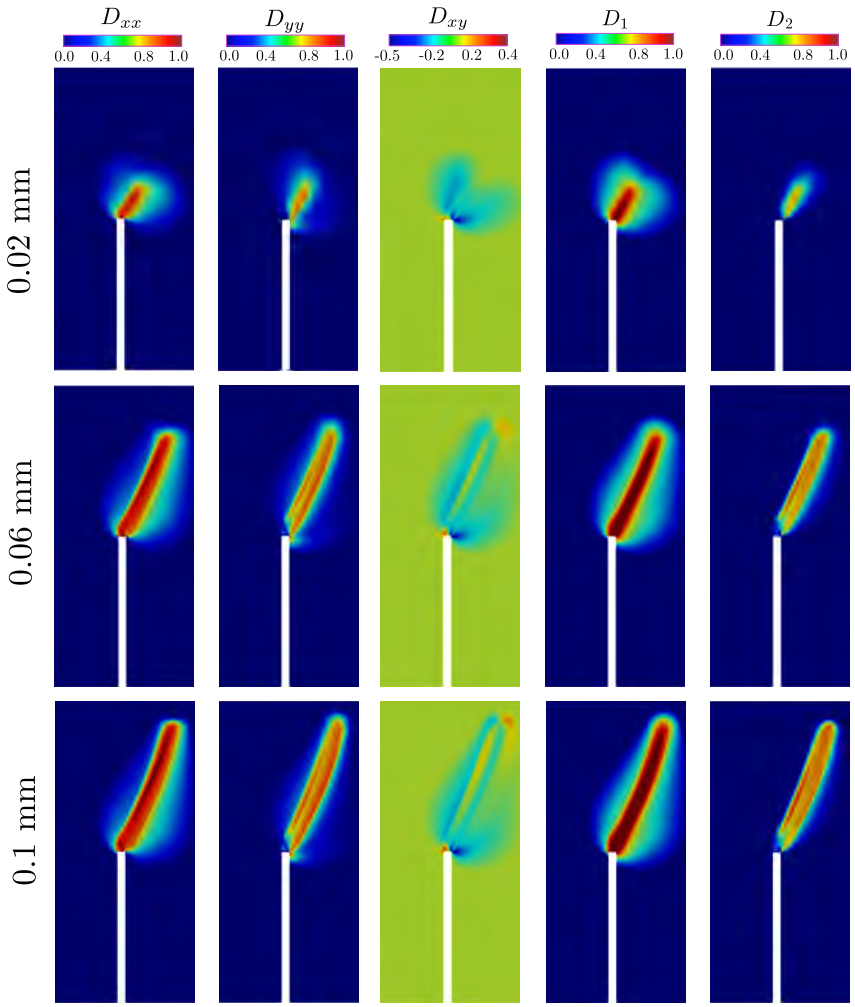

Figure 12: Three-point bending test – Evolution of damage patterns for different levels of CMOD. From left to right, the components D_{xx}, D_{yy} and D_{xy} of the damage tensor are depicted in the first three columns. The last two columns show the corresponding damage principal values D_1 and D_2.

5.3. Hexagonal specimen under non-proportional loading

To illustrate a scenario where isotropic and anisotropic damage models may yield different results, we suggest examining the response of an hexagonal specimen submitted to non proportional loading. The aim of this purely numerical test-case is solely to highlight how the ENLG formulation with anisotropic non-local interactions and anisotropic damage behavior can result in distinct damage paths compared to an isotropic ENLG model, particularly concerning the influence of preexisting directional damage on damage propagation in a different direction. It is important to note that our intention is not to assert the superiority, if any, of anisotropic damage models over isotropic ones.

Fassin et al. (2019) showed that anisotropic and isotropic damage models may yield significantly different results regarding damage patterns under non-proportional loading conditions. However, their analysis was limited to the impact of anisotropic damage behavior in structural simulations, while the non-local interactions remained isotropic and constant. In the example presented below, we focus on how the induced anisotropic damage behavior leads to evolving anisotropic non-local interactions through the ENLG model and how this can affect the damage patterns.

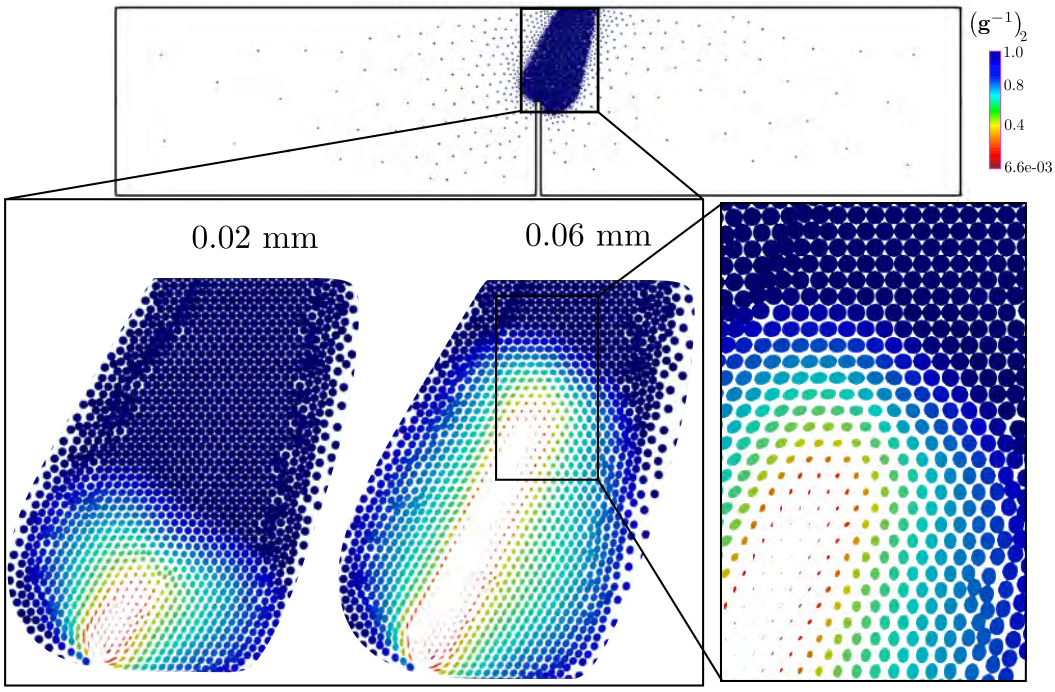

Figure 13: Three-point bending test – Evolution of interactions ellipses representing the tensor $\mathbf{g}^{-1} = \mathbf{H}^{-2}$ corresponding to two different CMOD levels (= 0.02 mm, 0.06 mm). The second (smaller) eigenvalue $(\mathbf{g}^{-1})_2$ is colored and represents the principal direction of the reduced interactions.

The geometry and boundary conditions are given in Figure 14 (bottom), along with the magnitude of the applied displacement for each step (Figure 14 (top)). The specimen is a regular hexagon with 50 mm side length, submitted to a non-proportional loading applied in three major steps: (*i*) Compression loading at Step A until $u_c = u_c^{max}$ to introduce a diffuse damage in the specimen; (*ii*) Unloading phase at Step B until $u_c = 0$ to release the compression load; (*iii*) Tension loading at Step C until $u_t = u_t^{max}$ to localize damage from the corners.

5.3.1. Damage models and material parameters

Three different models are employed for this example: the ENLG (evolving isotropic interactions) model coupled with a simple isotropic damage constitutive law (Ribeiro Nogueira et al., 2024), the ENLG (evolving anisotropic interactions) model coupled with the tensorial anisotropic damage law by Desmorat (2015), and the GNL (isotropic and constant interactions) model (Peerlings et al., 1996) coupled with the same anisotropic damage law.

In the isotropic case, damage is modeled through a scalar variable $D \in [0, 1]$ and the constitutive law reads $\boldsymbol{\sigma} = (1 - D)\mathbb{E} : \boldsymbol{\varepsilon} = \tilde{\mathbb{E}}^{\text{iso}} : \boldsymbol{\varepsilon}$. The damage criterion function remains the same as for the anisotropic model, whereas the isotropic damage evolution is considered as $D = 1 - \frac{\kappa_0}{\kappa} \exp\left(-B_t(\kappa - \kappa_0)\right)$, where B_t is a material parameter (see Appendix B for a comparison between isotropic and anisotropic damage models at the material point level). For all the models, the non-local Von Mises equivalent strain with $k = 10$ was used to ensure a larger damage threshold in the compression phase compared to the Mazars' strain. To compare, at least qualitatively, the numerical results obtained with the different models, the remaining material parameters used for simulating this test case were calibrated to provide a similar initial damage state right after Step A. In particular, the elastic properties are set to $\{E, \nu\} = \{17\,000\,\text{N/mm}^2, 0.18\}$ for all the models. Similarly, the initial length scale parameter is $c = 12\,\text{mm}^2$ for all the models. The remaining parameters are chosen as $\{\kappa_0, B_t\} = \{9.5 \times 10^{-5}, 700\}$ for the isotropic ENLG model, $\{\kappa_0, S, s, B\} = \{7.0 \times 10^{-5}, 9.25 \times$

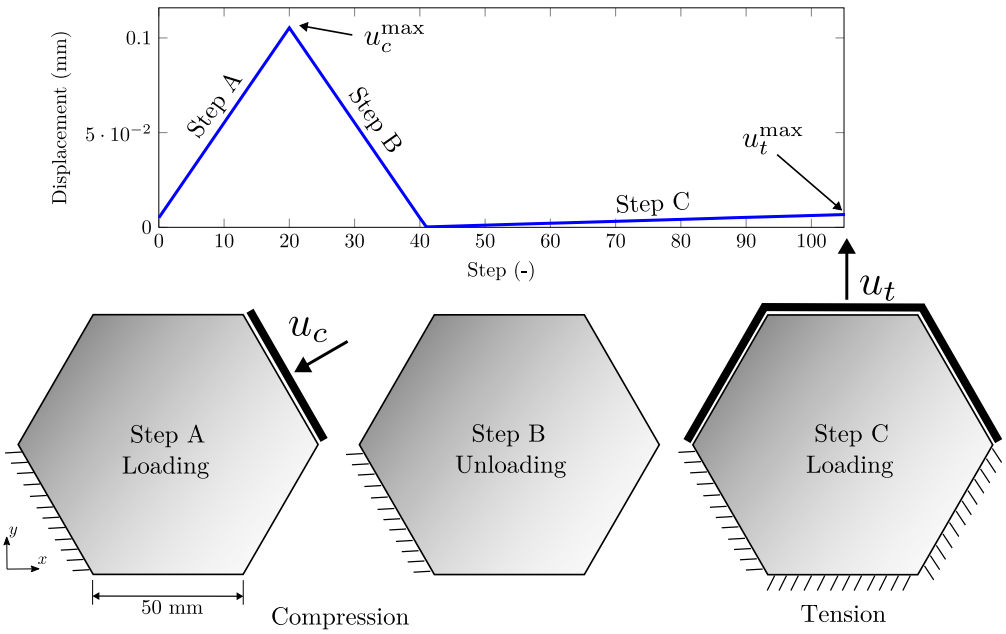

Figure 14: Hexagonal specimen test – Geometry and boundary conditions (thickness = 100 mm).

$10^{-5}, 4.9, 1.2\}$ for the anisotropic ENLG model, and $\{\kappa_0, S, s, B\} = \{8.0 \times 10^{-5}, 5.8 \times 10^{-5}, 4.9, 1.3\}$ for the GNL anisotropic model. The residual interactions parameter is set to $\xi = 0$ for all the models.

5.3.2. Representative results

Damage evolution. The damage patterns obtained for each model are depicted in Figure 15 for four loading steps. For the anisotropic damage behavior, only the first principal damage component is represented, whereas the scalar damage variable is used for the isotropic model.

At Step 20 ($u_c = u_c^{\max}$) one can observe that, for all the models, a diffuse damage takes place in the central part of the specimen due to the extensions perpendicular to the loading direction. At Step 80, a horizontal damage band starts to grow from the corners due to the applied tension loading in the vertical direction. Until this point, the three models give very similar results. Pronounced differences can be noticed from Step 86 to Step 101. In the case of the anisotropic ENLG model, the horizontal damage bands become curved when crossing the central zone, which was previously damaged during the compression load. On the contrary, the damage bands are not affected by the preexisting damage in the central region for the ENLG isotropic and GNL anisotropic models, resulting in a almost fully horizontal damage pattern. In this second case, this behavior mainly results from constant isotropic non-local interactions, leading to the diffusion of damage.

Anisotropic interactions and damage-dependent Riemannian metric acting as a structural tensor. To gain further insight into why the damage patterns become curved for the ENLG anisotropic model, it is useful to study how the induced anisotropic behavior affects the evolution of the non-local interactions during the loading steps.

Figure 16 shows, for each element, the plane defined by the first damage eigenvector (i.e., the eigenvector associated with the damage eigenvalue D_1) for the ENLG anisotropic damage model, which can be considered representative of elementary “pseudo-cracks” developing within each element. One can observe that in the diffuse damage phase (Step A), the equivalent “pseudo-cracks" are parallel to the loading (compression) direction. This observation also holds for the GNL anisotropic model; however, this is not true for the

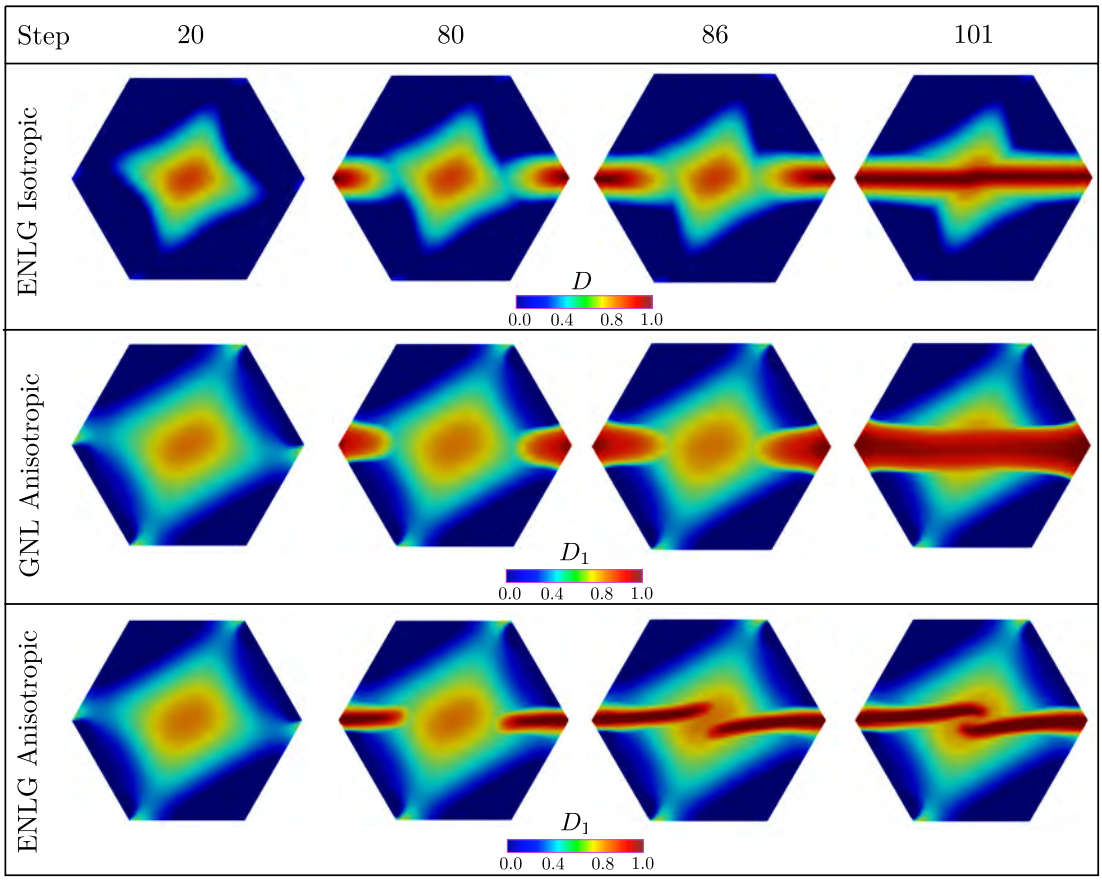

Figure 15: Hexagonal specimen test – Damage patterns obtained for the different models during the test.

ENLG isotropic case, given that the notions of damage principal directions cannot be represented with a scalar variable. Then, during the tensile loading phase in the vertical direction, equivalent “pseudo-cracks" are horizontal and start to rotate during damage propagation in the central regions of the specimen (Figure 16 right) for the ENLG anisotropic model as an effect of the preexisting damage generated in the compression phase.

The key point here is that the anisotropic damage behavior induces anisotropic non-local interactions by the means of the inverse of the metric $\mathbf{g}^{-1}$ for the ENLG anisotropic model (equation (13)). It acts as a structural tensor (see equations (6) and (7)), defining the impact of the damage-induced orthotropic material symmetry in the non-local contribution of the free-energy. This is also confirmed by the analysis of interaction ellipses and the corresponding damage patterns for different loading steps (Figure 17). One observes that, at Step 20, the interaction ellipses are, again, oriented in the direction of crack propagation and compressed perpendicular to it.

This creates an induced internal structure with a preferential direction of damage propagation, which affects the damage pattern during the subsequent tension load. Such behavior is typically obtained for materials with intrinsic (initial) anisotropy (Teichtmeister et al., 2017; Gültekin et al., 2018; Li and Maurini, 2019; Gerasimov and De Lorenzis, 2022; Pranavi et al., 2023; Wu et al., 2015; Jin and Arson, 2018; Forghani et al., 2019; Yin et al., 2020; Lu and Guo, 2022). The main difference with the previously cited works is that, here, the material undergoes a transition from isotropic to anisotropic behavior, and the influence of such a damage nature on non-local interactions is naturally taken into account by the evolving damage-dependent metric $\mathbf{g}$.

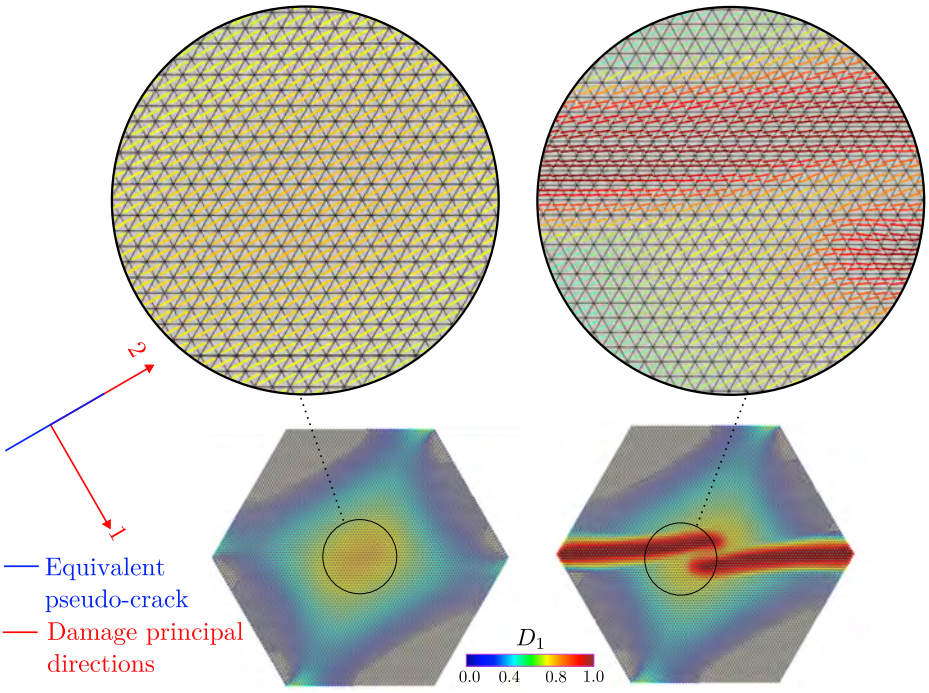

Figure 16: Hexagonal specimen test – Straight lines colored by D_1 values representing equivalent cracks perpendicular to damage first principal direction.

5.4. Toward 3D simulations – Mixed-mode 3D three-point bending test

The developments regarding the ENLG anisotropic model presented in this contribution can be readily extended to 3D. For illustrative purposes, let us consider the 3D simulation of a mixed-mode three-point bending test. A relatively coarse mesh ($l_e = 1.0, \text{mm}$ in the refined region, with 121 021 elements and 66 000 degrees of freedom) was generated. The material parameters for this test are chosen as $\{E, \nu, c, \kappa_0, S, s, B\} = \{38\,000\,\text{MPa}, 0.2, 4\,\text{mm}^2, 6 \times 10^{-4}, 2.71 \times 10^{-4}, 4.9, 5/3\}$. Moreover, the residual interactions parameter was set to $\xi = 0.0005$.

Damage evolution. Figure 18 displays the maps of the six damage components of the symmetric damage tensor in the central region of the beam. Consistent with observations from the 2D simulation of the same test, the damage band exhibits an orientation to the right of the notch. It can be clearly observed that the component D_{zz} remains considerably smaller than D_{xx} and D_{yy} across most regions. This confirms that major damage mechanisms take place in the plane $x - y$. Additionally, Figure 19 shows the maps of the corresponding three eigenvalues of the damage tensor. Similar to the 2D simulation, the first eigenvalue D_1 indicates that an equivalent "pseudo-crack" appears, which is associated to the damage principal direction.

On the scalability of the model. This 3D simulation highlights a disadvantage of the model. As explained earlier, achieving converged results requires very fine meshes in the simulations. For instance, in the 2D simulation of the three-point bending test, a refinement level of $l_e = 0.1, \text{mm}$ was necessary to achieve a converged structural response consistent with the reference experimental results. In 2D, this resulted in a mesh containing 178 476 elements (approximately 260 000 degrees of freedom) and a "reasonable" computational time. However, for a 3D simulation of the same experimental test, using a mesh with $l_e = 0.1, \text{mm}$ in the refined region leads to a number of degrees of freedom exceeding 10 million. Consequently, the analysis becomes computationally prohibitive with the sequential solver employed in this work. The use of parallel solving techniques should be considered in this case. Moreover, while local refinement has been employed in

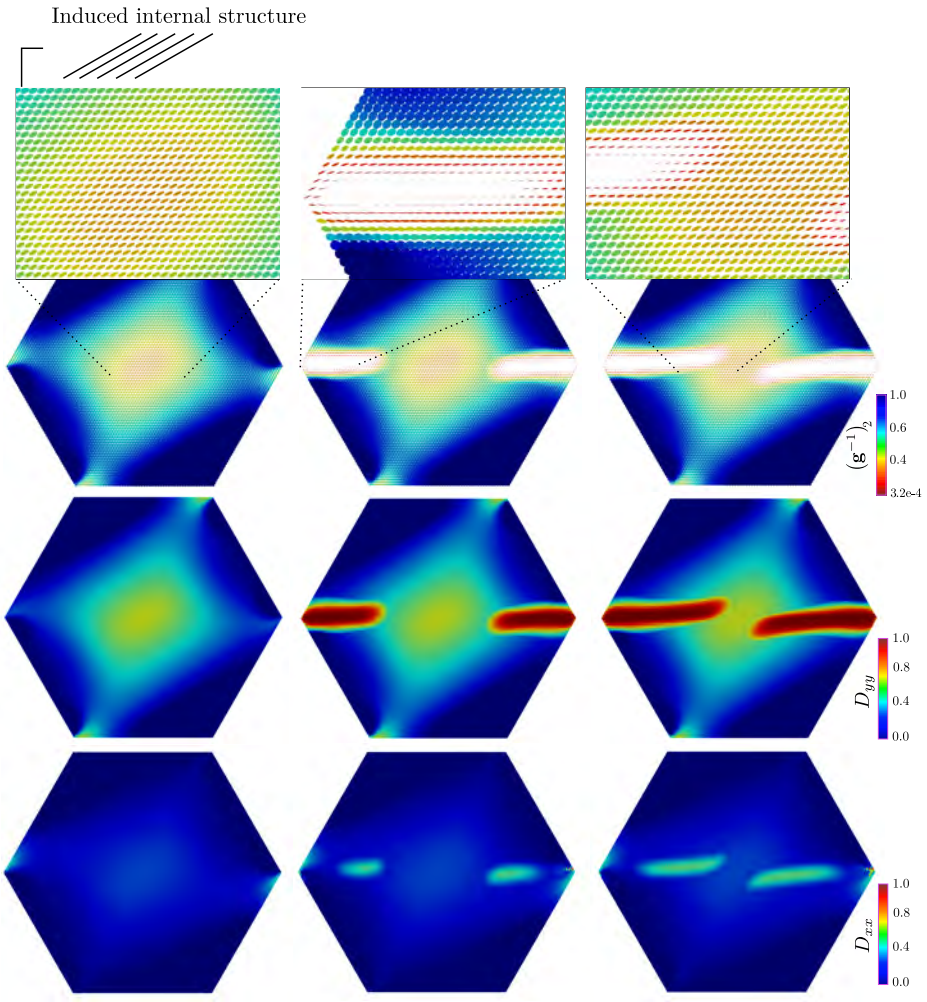

Figure 17: Hexagonal specimen test – First row shows the evolution of interactions ellipses representing the tensor $\mathbf{g}^{-1} = \mathbf{H}^{-2}$ corresponding to three different steps (20,75 and 95) of the applied loading. The second (smaller) eigenvalue $(\mathbf{g}^{-1})_2$ is colored and represents the principal direction of the reduced interactions. Second and third rows depict the corresponding damage patterns of components D_{yy} and D_{xx} of the damage tensor.

this contribution, in practical scenarios, the crack path is not known *a priori*. Mesh adaptation techniques could thus become useful for the simulation of larger-scale structures.

6. Conclusions

The gradient-enhanced Eikonal model has been successfully employed to regularize a tensorial anisotropic damage law based on Ladevèze's damage variable $\mathbf{H}$. This model was chosen for the sake of providing an example, but different second-order damage models (eventually using the damage variable $\mathbf{D}$ instead of $\mathbf{H}$) can be coupled with the ENLG regularization without modifying the general framework.

The variational formulation of the coupled problem was established by linking $\mathbf{H}$ and the damage-dependent Riemannian metric $\mathbf{g}$ from the ENLG model. A procedure for considering residual non-local interactions was proposed. The framework is applicable to the regularization of anisotropic damage mechanics models in both 2D and 3D analyses.

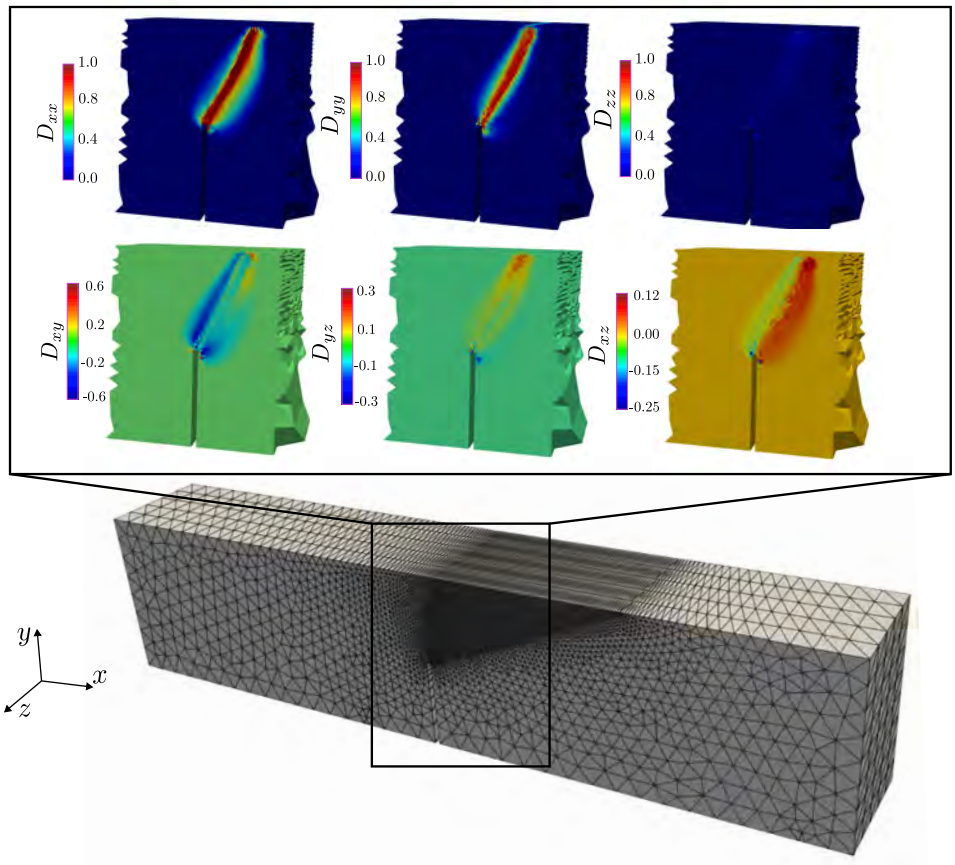

Figure 18: 3D three-point bending test – Maps of the six components (D_{xx}, D_{yy}, D_{zz}, $D_{xy} = D_{yx}$, $D_{xz} = D_{zx}$, $D_{yz} = D_{zy}$) of the damage tensor $\mathbf{D}$.

The developed plane stress model was utilized to simulate three different test cases in 2D. In the L-shape test, the numerically obtained structural response exhibited quasi-brittle behavior consistent with experimental observations. Additionally, the numerically obtained damage patterns closely matched the experimental one. Mesh convergence was obtained with a fine mesh.

In the simulation of a mixed-mode three-point bending test, the damage-induced anisotropic character of non-local interactions was enhanced. Tensor visualization using ellipses highlighted the role of the inverse of the metric (*i.e.*, of damage) in reducing non-local interactions when damage occurs. A realistic damage pattern was obtained, while maintaining agreement with experimental results in terms of the Force vs. CMOD curve. The eigenvectors of the damage tensor provided crucial information about equivalent "pseudo-crack" growth direction and propagation.

A purely numerical test case was then proposed to highlight a few differences between models with isotropic and anisotropic non-local interactions. The response of a hexagonal specimen under non-proportional loading was studied. It was demonstrated that, as expected, the tensorial damage behavior induces an internal structure based on the material symmetry (initially isotropic material becomes orthotropic when damage develops). In the case of the ENLG model coupled with anisotropic damage, damage patterns become curved when crossing a previously damaged region in a specific preferential direction thanks to the anisotropic interaction kernel induced by the damage-dependent Riemannian metric.

Finally, a first 3D simulation was briefly presented to highlight that using the proposed formulation in such a setting is already possible. However, additional numerical developments, particularly concerning parallel

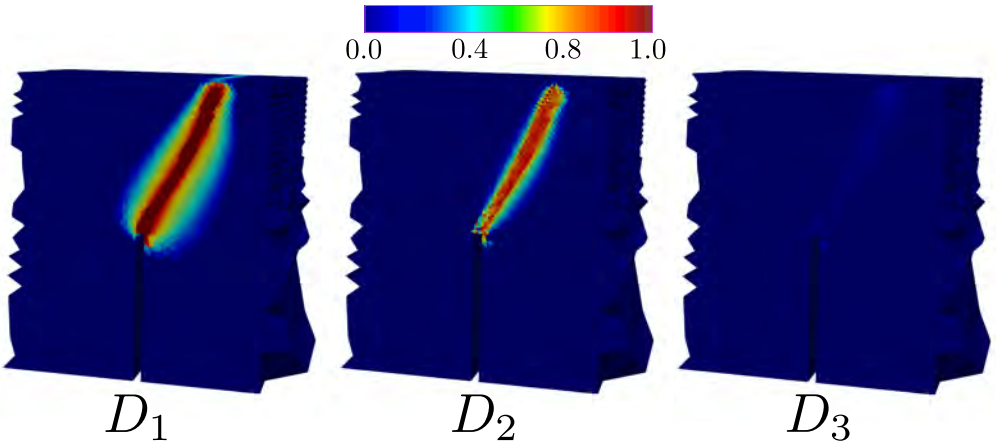

Figure 19: 3D Mixed-mode three-point bending test — Maps of the three eigenvalues (D_1,D_2,D_3) of the damage tensor $\mathbf{D}$.

solving techniques using domain decomposition methods (see, e.g., Badri et al. (2021); Badri and Rastiello (2023)) become necessary to perform damage mechanics simulations with meshes that are fine enough to achieve mesh-converged results (millions of degrees of freedom). Additionally, mesh adaptation techniques could become useful, especially when crack paths are unknown.

The ENLG model coupled with anisotropic damage exhibited intrinsic characteristics, such as anisotropic damage and evolving non-local interactions, important for reproducing experiments outlined as “distinctive” in (Bažant et al., 2022a; Bažant and Nguyen, 2023). Future investigations should focus on simulating these tests and also on verifying the capabilities of the proposed formulation in addressing size-effects in notched and unnotched three-point bending tests (Grégoire et al., 2013). Adaptations to the behavior law, such as considering residual stresses, may also enhance fitting to both ultimate force and post-peak behavior simultaneously.

The damage re-localization features of the ENLG formulation and directional information provided by the anisotropic damage model could also be useful in developing modeling strategies that explicitly represent the transition from continuum damage to fracture (see, e.g., Simone et al. (2003b); Negi and Kumar (2022)).

Finally, in scenarios involving multi-physics coupling, such as diffusion in cracked structures (e.g., estimating leakage rates in containment walls), the anisotropic damage framework presented here can be useful or predicting the evolution of the material’s anisotropic permeability/diffusion properties (Bary et al., 2000; Rastiello et al., 2015, 2016).

7. Acknowledgments

This work is supported by a public grant overseen by the French National research Agency (ANR) as part of the "Investissements d’Avenir" program, through the "ADI 2021" project funded by the IDEX Paris-Saclay, ANR-11-IDEX-0003-02. The University of Molise, Italy, is also acknowledged for its financial support.

G. Rastiello is supported by the SEISM Institute, France (https://www.institut-seism.fr/en/).

Appendix A. Implicit damage model integration at Gauss point level

Constitutive model integration is performed once one has computed $\boldsymbol{u}^{h,k+1}$ and $\bar{e}^{h,k+1}$. These fields being knows, , the goal is to determine $\mathbf{H}$ and $\tilde{\mathbb{E}}$. For brevity, the global iteration index $(k+1)$ and the subscript

h are omitted. Additionally, for ease of variable initialization, the model is reformulated using the tensor $\mathbf{A} = \mathbf{H} - \mathbf{I}$. Consequently, in the undamaged state, $\mathrm{tr}\,(\mathbf{A}) = 0$. The evolution of damage is thus calculated as follows:

(*i*) Compute the total strain $\boldsymbol{\varepsilon} = \boldsymbol{\varepsilon}_n + \Delta\boldsymbol{\varepsilon}$ based on the last computed displacement.

(*ii*) Compute $T_{X,n} = \frac{\mathrm{tr}\,\boldsymbol{\sigma}_n}{\sigma_{eq,n}}$ to obtain the triaxility function $R_{v,n}$ at the previous step.

(*iii*) Compute a trial of the criterion function:

$$f_{\mathrm{try}} = \bar{e} - \kappa_n \qquad \kappa_n = \kappa_0 + SR_v^s \mathrm{tr}\,(\mathbf{A}_n) \qquad \bar{e} = \bar{e}^{k+1} \tag{A.1}$$

- If $f_{\mathrm{try}} < 0$, there is no damage evolution, *i.e.*, $\mathbf{A}^{k+1} = \mathbf{A}_n$.
- Otherwise, an iterative procedure is employed to find a solution satisfying $f(\mathbf{A}) = 0$. In this case (we denote with letter i the local sub-iterations):
  - The damage rate direction tensor $\mathbf{P}_n$ is defined after having computed the total (or effective) strain tensor at previous time step.
  - One then looks for $\delta\mathbf{A}^{i+1}$ such that:

$$f^{i+1} \approx f^i + \left.\frac{df}{d\mathbf{A}}\right|_i : \delta\mathbf{A}^{i+1} = f^i - SR_v^s \mathrm{tr}\,(\delta\mathbf{A}^{i+1}) = 0 \tag{A.2}$$

  with:

$$f^i = \bar{e} - \kappa_0 - SR_v^s \mathrm{tr}\,(\mathbf{A}^i) \qquad \mathrm{tr}\,(\delta\mathbf{A}^{i+1}) = \delta\lambda^{i+1}\,\mathrm{tr}\,\mathbf{P}_n \tag{A.3}$$

  Finally, one has:

$$\delta\lambda^{i+1} = \frac{\bar{e} - \kappa_0}{SR_v^s \mathrm{tr}\,\mathbf{P}_n} - \frac{\mathrm{tr}\,(\mathbf{A}^i)}{\mathrm{tr}\,\mathbf{P}_n} \tag{A.4}$$

  and then:

$$\mathbf{A}^{i+1} = \mathbf{A}^i + \delta\lambda^{i+1}\mathbf{P}_n \tag{A.5}$$

  - Once local convergence is achieved, one sets:

$$\mathbf{A}^{k+1} = \mathbf{A}^{i+1} \tag{A.6}$$

(*iv*) Update the Ladevèze damage variable at convergence:

$$\mathbf{H}^{k+1} = \mathbf{A}^{k+1} + \mathbf{I} \tag{A.7}$$

compute the effective Hooke's tensor $\tilde{\mathbb{E}} = \tilde{\mathbb{E}}\,(\mathbf{H}^{k+1})$ from equation 29, and compute the stress tensor $\boldsymbol{\sigma}^{k+1} = \tilde{\mathbb{E}}^{k+1} : \boldsymbol{\varepsilon}$. Finally, the tensorial damage variable $\mathbf{D}^{k+1}$ is computed.

Plane stress modifications in constitutive behavior integration. While the general process for integrating constitutive behavior remains largely unchanged, there are specific modifications introduced for plane stress conditions. These adjustments include:

(*i*) The same procedure as described earlier is applicable to $\boldsymbol{\varepsilon}_2$.

(*ii*) Triaxility is computed with the two-dimensional stress tensor $\boldsymbol{\sigma}$.

(*iii*) The variation in the damage multiplier is determined by:

$$\delta\lambda = \frac{\bar{e}_{n+1} - \kappa_0}{SR_v^s\,(\mathrm{tr}\,\mathbf{P}_{\mathbf{2},n} + \langle\tilde{\varepsilon}_{z,n}\rangle\,)} - \frac{\mathrm{tr}\,(\mathbf{A}_{\mathbf{2}}^i) + rH_z}{\mathrm{tr}\,\langle\tilde{\boldsymbol{\varepsilon}}_{\mathbf{2},n}\rangle + \langle\tilde{\varepsilon}_{z,n}\rangle} \tag{A.8}$$

where $\mathbf{A_2} = \mathbf{H_2} - \mathbf{I_2}$. Thus, one has:

$$\delta\mathbf{A_2} = \delta\lambda\,\langle\tilde{\boldsymbol{\varepsilon}}_{\mathbf{2},n}\rangle \qquad \delta A_z = \langle\tilde{\varepsilon}_{z,n}\rangle \tag{A.9}$$

(*iv*) At convergence, update the Ladevèze damage variable $\mathbf{H}_{\mathbf{2},n+1} = \mathbf{r}\mathbf{H}^{i+1}_{\mathbf{2},n+1} + \mathbf{I_2}$, compute the two-dimensional effective Hooke's tensor $\tilde{\mathbb{E}}^{\star}_{n+1} = \tilde{\mathbb{E}}^{\star}\left(\mathbf{H}_{\mathbf{2},n+1}, H_{z,n+1}\right)$ from equation 40, and calculate the stress tensor $\boldsymbol{\sigma}_{n+1} = \tilde{\mathbb{E}}^{\star}_{n+1} : \boldsymbol{\varepsilon}_{\mathbf{2},n+1}$. Finally, compute the tensorial damage variable $\mathbf{D}_{\mathbf{2},n+1} = \mathbf{I_2} - \mathbf{H}^{-2}_{\mathbf{2},n+1}$ and $D_{z,n+1} = 1 - H^{-2}_{z,n+1}$.

Representative local responses obtained using the chosen anisotropic damage model at the integration point level are presented in Appendix B.

Appendix B. Representative local responses of the anisotropic damage model

Representative responses simulated using the anisotropic damage model discussed in Section 2 are provided. These numerical results are obtained through `mtest`, an open-source Python tool distributed alongside `Mfront`. This tool enables the simulation of complex loading conditions at the integration point level, facilitating the testing and validation of constitutive law implementations without the need for a finite element solver.

Appendix B.1. Pure tension/compression

Figure B.20 (top) displays a typical response obtained with the anisotropic damage model under tension and compression. The parameters used for this test are the ones proposed in (Desmorat, 2015), i.e., $\{E, \nu, \kappa_0, S, s, B\} = \{37\,000\,\text{MPa}, 0.2, 9e-5, 1.45e-4, 4.9, 5/3\}$. The tension-compression dissimetry behavior is illustrated in Figure B.20 (top-right). This dissimetry arises due to micro-cracks developing as a consequence of extensions perpendicular to the applied load, induced by the Poisson's effect. As a result, damage variable components evolve more slowly under compression conditions.

Figure B.20 (bottom) depicts the corresponding evolution of the damage variable under tension and compression. In uniaxial tension along x, micro-cracks develop perpendicular to the applied load, as qualitatively represented in Figure B.20 (bottom-left). Consequently, the damage component D_{xx} rapidly evolves to unity, reflecting the direct tension applied in this direction. Meanwhile, due to Poisson's effect, shrinkage occurs on y and z (resulting in negative strains), causing the damage components D_{yy} and D_{zz} to remain unchanged. In contrast, uniaxial compression along x leads to micro-cracks developing parallel to the applied load, as illustrated in Figure B.20 (bottom-right). Extensions (resulting in positive strains) appear on y and z, causing the damage component D_{xx} to remain static. The damage principal directions align with y and z but are associated with indirect extensions. Consequently, D_{yy} and D_{zz} are equal and evolve much more slowly than in the direct tension case.

Appendix B.2. Non-proportional loading

Non-proportional loading is simulated here to illustrate one of the advantages of employing the anisotropic damage model over an isotropic one. The total loading time is discretized into 2000 pseudo-time steps. A non-proportional load is applied, initially imposing an increasing strain component ε_{xx} until step 500 (see Figure B.21). Subsequently, an unloading phase occurs until step 1000, where $\varepsilon_{xx} = 0$ and $\sigma_{xx} = 0$ (see Figure B.21). From step 1000 until 2000 (end of the simulation), an increasing strain component ε_{yy} is applied (depicted by the red curve in Figure B.21), with no conditions imposed on the other components.

Isotropic vs anisotropic models. The stress-strain response obtained with the isotropic model is shown in Figure B.22 (top-left). Elastic parameters are consistent with the ones previously used: $E = 37000$ MPa and $\nu = 0.2$. Moreover, $\kappa_0 = 1e-4$ and the exponential parameter $B_t = 1000$, which are typically used for the isotropic damage evolution considered here. Figure B.22 (top-right) illustrates that the response follows the same effective modulus during unloading on x and loading on y. This is expected since, once damaged, all components of the effective Hooke's tensor $\tilde{\mathbb{E}}^{\text{iso}}$ are affected by the same factor $(1 - D)$. Consequently, $\tilde{\mathbb{E}}^{\text{iso}}$ remains isotropic.

On the contrary, the Hooke's tensor evolves from isotropic to orthotropic in the case of the tensorial damage model used here. The stress-strain response for the loading case presented is depicted in Figure B.22 (bottom-left). For comparison purposes, elastic material parameters are kept consistent with those used for the isotropic model. The other parameters are taken as in section 4.2. The response does not follow the same effective modulus during reloading on the y direction, reflecting the induced anisotropy due to damage. The effective Hooke's tensor components evolve differently as damage takes place. For instance, from the expression of the effective Hooke's tensor (Equation 29), one observes that:

$$\tilde{E}_{1111} = 2G\left[H_{11}^{-1}H_{11}^{-1} - \frac{H_{11}^{-2}H_{11}^{-2}}{\operatorname{tr}\mathbf{H}^{-2}}\right] + \frac{3K}{\operatorname{tr}\mathbf{H}^{2}} \qquad \tilde{E}_{2222} = 2G\left[H_{22}^{-1}H_{22}^{-1} - \frac{H_{22}^{-2}H_{22}^{-2}}{\operatorname{tr}\mathbf{H}^{-2}}\right] + \frac{3K}{\operatorname{tr}\mathbf{H}^{2}} \tag{B.1}$$

are naturally different once damage occurs. As illustrated in Figure B.22 (bottom-right), the components $\tilde{E}_{1111}$ and $\tilde{E}_{2222}$ are initially the same in the elastic phase (*i.e.*, when the material is isotropic). However, they evolve differently as a function of the damage state. This induced anisotropic behavior is essential for accurately capturing the anisotropic nature of non-local interactions, which is represented in this work by a damage-dependent Riemannian metric.

References

Amani, J., 2023. A transient-anisotropic gradient-enhanced damage model with displacement smoothing for failure analysis in quasi-brittle materials. Ph.D. thesis. Technische Universiteit Delft.

Badri, M.A., Rastiello, G., 2023. Hpc finite element solvers for phase-field models for fracture in solids, in: Rossi, P., Tailhan, J.L. (Eds.), Numerical Modeling Strategies for Sustainable Concrete Structures, Springer International Publishing, Cham. pp. 22–32.

Badri, M.A., Rastiello, G., Foerster, E., 2021. Preconditioning strategies for vectorial finite element linear systems arising from phase-field models for fracture mechanics. Computer Methods in Applied Mechanics and Engineering 373, 113472.

Bary, B., Bournazel, J.P., Bourdarot, E., 2000. Poro-Damage Approach Applied to Hydro-Fracture Analysis of Concrete. Journal of Engineering Mechanics 126, 937–943. doi:10.1061/(ASCE)0733-9399(2000)126:9(937).

Bažant, Z., Oh, B., 1983. Microplane model for fracture analysis of concrete structures. Proc. Symposium on the Interaction of Non-nuclear Munitions with Structures, held at US Air Force Academy, Colorado Springs. (publ. by McGregor and Werner, Washington DC) .

Bažant, Z., Prat, P.C., 1988. Microplane model for brittle-plastic material: I. theory. ASCE J. Eng. Mech 114, 1672–1688.

Bažant, Z.P., 1984. Microplane Model for Strain-controlled Inelastic Behaviour, in: Mechanics of Engineering Materials. c. s. desai and r. h. gallagher ed.. John Wiley & Sons Ltd, pp. 46 – 56.

Bažant, Z.P., Dönmez, A.A., Nguyen, H.T., 2022a. Précis of gap test results requiring reappraisal of line crack and phase-field models of fracture mechanics. Engineering Structures 250, 113285.

Bažant, Z.P., Gambarova, P.G., 1984. Crack shear in concrete: Crack band microplane model. Journal of Structural Engineering 110, 2015–2035.

Bažant, Z.P., Nguyen, H.T., 2023. Proposal of m-Index for Rating Fracture and Damage Models by Their Ability to Represent a Set of Distinctive Experiments. Journal of Engineering Mechanics 149, 04023047.

Bažant, Z.P., Nguyen, H.T., Abdullah Dönmez, A., 2022b. Critical Comparison of Phase-Field, Peridynamics, and Crack Band Model M7 in Light of Gap Test and Classical Fracture Tests. Journal of Applied Mechanics 89, 061008. doi:10.1115/1.4054221.

Bažant, Z.P., Xiang, Y., Prat, P.C., 1996. Microplane Model for Concrete. I: Stress-Strain Boundaries and Finite Strain. Journal of Engineering Mechanics 122, 245–254. doi:10.1061/(ASCE)0733-9399(1996)122:3(245).

Berthaud, Y., 1991. Damage measurements in concrete via an ultrasonic technique. Part I Experiment. Cement and Concrete Research 21, 73–82.

Boehler, J.P. (Ed.), 1987. Applications of Tensor Functions in Solid Mechanics. Springer Vienna, Vienna. doi:10.1007/978-3-7091-2810-7.

Chaboche, J., 1982. The concept of effective stress applied to elasticity and to viscoplasticity in the presence of anisotropic damage., in: Mechanical Behavior of Anisotropic Solids / Comportment Méchanique des Solides Anisotropes: Proceedings of the Euromech Colloquium 115 Villard-de-Lans, June 19-22, 1979 / Colloque Euromech 115 Villard-de-Lans, 19-22 juin 1979. Springer Netherlands, pp. 737–760.

Chambart, M., 2009. Endommagement anisotrope et comportement dynamique des structures en béton armé jusqu'à la ruine. Ph.D. thesis. École normale supérieure de Cachan - ENS Cachan.

Cordebois, J., Sidoroff, F., 1982. Anisotropic damage in elasticity and plasticity. Journal de Mécanique Théorique et Appliquée, numéro spécial , 45–60.

de Borst, R., 1987. Computation of post-bifurcation and post-failure behavior of strain-softening solids. Computers & Structures 25, 211–224. URL: https://www.sciencedirect.com/science/article/pii/0045794987901441, doi:https://doi.org/10.1016/0045-7949(87)90144-1.

De Vree, J., Brekelmans, W., van Gils, M., 1995. Comparison of nonlocal approaches in continuum damage mechanics. Computers & Structures 55, 581–588.

Desmorat, R., 2004. Modèle d' endommagement anisotrope avec forte dissymétrie traction/compression. In : 5è journées du Regroupement Francophone pour la Recherche et la Formation sur le Béton (RF2B), 5-6 July, Liège, Belgium .

Desmorat, R., 2015. Anisotropic damage modeling of concrete materials. International Journal of Damage Mechanics 25, 818–852.

Desmorat, R., Gatuingt, F., 2007. Introduction of an internal time in nonlocal integral theories. Internal report LMT .

Desmorat, R., Gatuingt, F., Jirasek, M., 2015. Nonlocal models with damage-dependent interactions motivated by internal time. Engineering Fracture Mechanics 142, 255–275.

Desmorat, R., Gatuingt, F., Ragueneau, F., 2007. Nonlocal anisotropic damage model and related computational aspects for quasi-brittle materials. Engineering Fracture Mechanics 74(10), 1539–1560.

Fassin, M., Eggersmann, R., Wulfinghoff, S., Reese, S., 2019. Gradient-extended anisotropic brittle damage modeling using a second order damage tensor – Theory, implementation and numerical examples. International Journal of Solids and Structures 167, 93–126.

Forest, S., 2009. Micromorphic Approach for Gradient Elasticity, Viscoplasticity, and Damage. Journal of Engineering Mechanics 135, 117–131.

Forghani, A., Poursartip, A., Vaziri, R., 2019. An orthotropic non-local approach to modeling intra-laminar damage progression in laminated composites. International Journal of Solids and Structures 180-181, 160–175.

Geers, M., de Borst, R., Brekelmans, W., Peerlings, R., 1998. Strain-based transient-gradient damage model for failure analyses. Computer Methods in Applied Mechanics and Engineering 160, 133–153.

Gerasimov, T., De Lorenzis, L., 2022. Second-order phase-field formulations for anisotropic brittle fracture. Computer Methods in Applied Mechanics and Engineering 389, 114403. doi:10.1016/j.cma.2021.114403.

Giry, C., Dufour, F., Mazars, J., 2011. Stress-based nonlocal damage model. International Journal of Solids and Structures 48, 3431–3443. URL: https://linkinghub.elsevier.com/retrieve/pii/S002076831100299X, doi:10.1016/j.ijsolstr.2011.08.012.

Grégoire, D., Rojas-Solano, L., Pijaudier-Cabot, G., 2013. Failure and size effect for notched and unnotched concrete beams. International Journal for Numerical and Analytical Methods in Geomechanics 37, 1434–1452.

Gálvez, J.C., Elices, M., Guinea, G.V., Planas, J., 1998. Mixed Mode Fracture of Concrete under Proportional and Nonproportional Loading. International Journal of Fracture 94, 267–284.

Gültekin, O., Dal, H., Holzapfel, G.A., 2018. Numerical aspects of anisotropic failure in soft biological tissues favor energy-based criteria: A rate-dependent anisotropic crack phase-field model. Computer Methods in Applied Mechanics and Engineering 331, 23–52. doi:10.1016/j.cma.2017.11.008.

Halm, D., Dragon, A., 1998. An anisotropic model of damage and frictional sliding for brittle materials. European Journal of Mechanics A/Solids 17(3), 439–460.

Hamilton, N., Cal, R.B., 2015. Anisotropy of the Reynolds stress tensor in the wakes of wind turbine arrays in Cartesian arrangements with counter-rotating rotors. Physics of Fluids 27, 015102.

Hecht, F., 2012. New development in freefem++. J. Numer. Math. 20, 251–265. URL: https://freefem.org/.

Helfer, T., Michel, B., Proix, J.M., Salvo, M., Sercombe, J., Casella, M., 2015. Introducing the open- source mfront code generator: Application to mechanical behaviours and material knowledge management within the pleiades fuel element modelling platform. Computers and Mathematics with Applications 70(5), 994–1023.

Jin, W., Arson, C., 2018. Anisotropic nonlocal damage model for materials with intrinsic transverse isotropy. International Journal of Solids and Structures 139-140, 29–42.

Jirásek, M., Suárez, F., 2016. Localization properties of Desmorat's anisotropic damage model. Computers & Structures 174, 139–153.

Krajcinovic, D., Fonseka, G.U., 1981. The continuous damage theory of brittle materials, parts i and ii. Journal of Applied Mechanics 48, 809–824.

Krajcinovic, D., Mastilovic, S., 1995. Some fundamental issues of damage mechanics. Mechanics of materials 21, 217–230.

Krayani, A., Pijaudier-Cabot, G., Dufour, F., 2009. Boundary effect on weight function in nonlocal damage model. Engineering Fracture Mechanics 76, 2217–2231.

Kuhl, E., Ramm, E., De Borst, R., 2000. An anisotropic gradient damage model for quasi-brittle materials. Computer Methods in Applied Mechanics and Engineering 183, 87–103.

Ladeveze, P., 1983. On an anisotropic damage theory. In Proc. CNRS Int. Coll 351 Villars-de-Lans, Failure crieria of structured media .

Lemaitre, J., 1996. A Course on Damage Mechanics. Springer Berlin Heidelberg, Berlin, Heidelberg.

Lemaitre, J., Desmorat, R., Sauzay, M., 2000. Anisotropic damage law of evolution. European Journal of Mechanics -

A/Solids 19, 187–208. URL: https://linkinghub.elsevier.com/retrieve/pii/S0997753800001613, doi:10.1016/S0997-7538(00)00161-3.
Leroux, A., 2012. Modèle multiaxial d'endommagement anisotrope: gestion numérique de la rupture et application à la ruine de structures en béton armé sous impacts. Ph.D. thesis. École normale supérieure de Cachan - ENS Cachan.
Li, B., Maurini, C., 2019. Crack kinking in a variational phase-field model of brittle fracture with strongly anisotropic surface energy. Journal of the Mechanics and Physics of Solids 125, 502–522.
Loiseau, F., 2023. Formulation of anisotropic damage in quasi-brittle materials and structures based on discrete element simulation. Ph.D. thesis. Université Paris-Saclay, ENS Paris-Saclay.
Loiseau, F., Oliver-Leblond, C., Verbeke, T., Desmorat, R., 2023. Anisotropic damage state modeling based on harmonic decomposition and discrete simulation of fracture. Engineering Fracture Mechanics 293, 109669.
Lu, X., Guo, X., 2022. An interactive orthotropic non-local damage model for progressive failure analysis of composite laminates. Composite Structures 295, 115841.
Lyu, Y., Pathirage, M., Nguyen, H.T., Bažant, Z.P., Cusatis, G., 2023. Dissipation mechanisms of crack-parallel stress effects on fracture process zone in concrete. Journal of the Mechanics and Physics of Solids 181, 105439. URL: https://www.sciencedirect.com/science/article/pii/S0022509623002430, doi:10.1016/j.jmps.2023.105439.
Maire, J., Chaboche, J., 1997. A new formulation of continuum damage mechanics (CDM) for composite materials. Aerospace Science and Technology 1, 247–257. doi:10.1016/S1270-9638(97)90035-3.
Marconi, F., 2022. Damage-fracture transition by an Eikonal-based gradient-type formulation for damage (-plastic) model. Ph.D. thesis. Université Paris-Saclay.
Masseron, B., Rastiello, G., Moës, N., Desmorat, R., 2023. Lip-field regularization of anisotropic damage, in: The Seventh International Conference on Computational Modeling of Fracture and Failure of Materials and Structures, Prague, Czech Republic. p. 234.
Mazars, J., 1984. Application de la mécanique de l' endommagement au comportement non linéaire et à la rupture du béton de structure. Ph.D. thesis. Université de Paris 6.
Murakami, S., 1988. Mechanical modeling of material damage. Journal of Applied Mechanics 55(2), 280–286.
Nagaraja, S., Römer, U., Matthies, H.G., De Lorenzis, L., 2023. Deterministic and stochastic phase-field modeling of anisotropic brittle fracture. Computer Methods in Applied Mechanics and Engineering 408, 115960.
Negi, A., Kumar, S., 2022. A continuous–discontinuous localizing gradient damage framework for failure analysis of quasi-brittle materials. Computer Methods in Applied Mechanics and Engineering 390, 114434.
Negi, A., Kumar, S., Poh, L.H., 2020. A localizing gradient damage enhancement with micromorphic stress-based anisotropic nonlocal interactions. International Journal for Numerical Methods in Engineering 121, 4003–4027.
Nguyen, G.D., 2011. A damage model with evolving nonlocal interactions. International Journal of Solids and Structures 48, 1544–1559.
Nguyen, H., Pathirage, M., Rezaei, M., Issa, M., Cusatis, G., Bažant, Z.P., 2020. New perspective of fracture mechanics inspired by gap test with crack-parallel compression. Proceedings of the National Academy of Sciences 117, 14015–14020. URL: https://pnas.org/doi/full/10.1073/pnas.2005646117, doi:10.1073/pnas.2005646117.
Nguyen, T.H., Bui, T.Q., Hirose, S., 2018. Smoothing gradient damage model with evolving anisotropic nonlocal interactions tailored to low-order finite elements. Computer Methods in Applied Mechanics and Engineering 328, 498–541.
Oliver, J., Huespe, A., Pulido, M., Blanco, S., 2004. Computational modeling of cracking of concrete in strong discontinuity settings. Computers and Concrete 1, 61–76.
Papa, E., Taliercio, A., 1996. Anisotropic damage model for the multiaxial static and fatigue behaviour of plain concrete. Engineering Fracture Mechanics 55, 163–179. URL: https://www.sciencedirect.com/science/article/pii/0013794496000045, doi:10.1016/0013-7944(96)00004-5.
Passelègue, F.X., Pimienta, L., Faulkner, D., Schubnel, A., Fortin, J., Guéguen, Y., 2018. Development and Recovery of Stress-Induced Elastic Anisotropy During Cyclic Loading Experiment on Westerly Granite. Geophysical Research Letters 45, 8156–8166. doi:10.1029/2018GL078434.
Peerlings, R., de Borst, R., Brekelmans, W., de Vree, J., 1996. Gradient-enhanced damage model for quasi-brittle materials. International Journal for Numerical Methods in Engineering 39, 391–403.
Peerlings, R., Massart, T., Geers, M., 2004. A thermodynamically motivated implicit gradient damage framework and its application to brick masonry cracking. Computer Methods in Applied Mechanics and Engineering 193, 3403–3417.
Peerlings, R.H.J., 1999. Enhanced damage modelling for fracture and fatigue. Ph.D. thesis. Technische Universiteit Eindhoven.
Pijaudier-Cabot, G., Dufour, F., 2010. Non local damage model: Boundary and evolving boundary effects. European Journal of Environmental and Civil Engineering 14, 729–749.
Pijaudier-Cabot, G., Haidar, K., Dubé, J.F., 2004. Non-local damage model with evolving internal length. International Journal for Numerical and Analytical Methods in Geomechanics 28, 633–652.
Pijaudier-Cabot, G., Bažant, Z.P., 1987. Nonlocal Damage Theory. Journal of Engineering Mechanics 113, 1512–1533.
Poh, L.H., Sun, G., 2017. Localizing gradient damage model with decreasing interactions. International Journal for Numerical Methods in Engineering 110, 503–522.
Pranavi, D., Rajagopal, A., Reddy, J.N., 2023. Phase field modeling of anisotropic fracture. Continuum Mechanics and Thermodynamics doi:10.1007/s00161-023-01260-6.
Ramtani, S., Berthaud, Y., Mazars, J., 1992. Orthotropic behavior of concrete with directional aspects: modelling and experiments. Nuclear Engineering and Design 133, 97–111. URL: https://linkinghub.elsevier.com/retrieve/pii/002954939290094C, doi:10.1016/0029-5493(92)90094-C.
Rastiello, G., Desmettre, C., Tailhan, J.L., Rossi, P., Charron, J.P., Dal Pont, S., 2016. Modeling of fluid leakage through multi-cracked RC structural elements using a numerical probabilistic cracking approach. Materials and Structures 49, 3095–3108.

doi:10.1617/s11527-015-0706-3.
Rastiello, G., Giry, C., Gatuingt, F., Desmorat, R., 2018. From diffuse damage to strain localization from an eikonal non-local (enl) continuum damage model with evolving internal length. Computer Methods in Applied Mechanics and Engineering 113, 1512–1233.
Rastiello, G., Oliveira, H.L., Millard, A., 2022. Path-following methods for unstable structural responses induced by strain softening: a critical review. Comptes Rendus. Mécanique 350, 205–236. doi:10.5802/crmeca.112.
Rastiello, G., Riccardi, F., Richard, B., 2019. Discontinuity-scale path-following methods for the embedded discontinuity finite element modeling of failure in solids. Computer Methods in Applied Mechanics and Engineering 349, 431–457.
Rastiello, G., Tailhan, J.L., Rossi, P., Dal Pont, S., 2015. Macroscopic probabilistic cracking approach for the numerical modelling of fluid leakage in concrete. Annals of Solid and Structural Mechanics 7, 1–16. URL: http://link.springer.com/10.1007/s12356-015-0038-6, doi:10.1007/s12356-015-0038-6.
Reese, S., Brepols, T., Fassin, M., Poggenpohl, L., Wulfinghoff, S., 2021. Using structural tensors for inelastic material modeling in the finite strain regime – A novel approach to anisotropic damage. Journal of the Mechanics and Physics of Solids 146, 104174. doi:10.1016/j.jmps.2020.104174.
Ribeiro Nogueira, B., Giry, C., Rastiello, G., Gatuingt, F., 2022. One-dimensional study of boundary effects and damage diffusion for regularized damage models. Comptes Rendus. Mécanique 350, 507–546.
Ribeiro Nogueira, B., Rastiello, G., Giry, C., Gatuingt, F., Callari, C., 2024. Differential geometry-based thermodynamics derivation of isotropic and anisotropic eikonal non-local gradient (ENLG) damage models using a micromorphic media framework. Engineering Fracture Mechanics 295, 109670. doi:10.1016/j.engfracmech.2023.109670.
Rojas-Solano, L.B., Grégoire, D., Pijaudier-Cabot, G., 2013. Interaction-based non-local damage model for failure in quasi-brittle materials. Mechanics Research Communications 54, 56–62.
Sarkar, S., Singh, I., Mishra, B., Shedbale, A., Poh, L., 2019. A comparative study and ABAQUS implementation of conventional and localizing gradient enhanced damage models. Finite Elements in Analysis and Design 160, 1–31.
Simone, A., Askes, H., Peerlings, R.H.J., Sluys, L.J., 2003a. Interpolation requirements for implicit gradient-enhanced continuum damage models. Communications in Numerical Methods in Engineering 19, 563–572. URL: http://doi.wiley.com/10.1002/cnm.597, doi:10.1002/cnm.597.
Simone, A., Askes, H., Sluys, L.J., 2004. Incorrect initiation and propagation of failure in non-local and gradient-enhanced media. International Journal of Solids and Structures 41, 351–363.
Simone, A., Wells, G.N., Sluys, L.J., 2003b. From continuous to discontinuous failure in a gradient-enhanced continuum damage model. Computer Methods in Applied Mechanics and Engineering 192, 4581–4607.
Teichtmeister, S., Kienle, D., Aldakheel, F., Keip, M.A., 2017. Phase field modeling of fracture in anisotropic brittle solids. International Journal of Non-Linear Mechanics 97, 1–21.
Thierry, F., Rastiello, G., Giry, C., Gatuingt, F., 2020. One-dimensional eikonal non-local (enl) damage models: Influence of the integration rule for computing interaction distances and indirect loading control on damage localization. Mechanics Research Communications 110, 103620.
Vandoren, B., Simone, A., 2018. Modeling and simulation of quasi-brittle failure with continuous anisotropic stress-based gradient-enhanced damage models. Computer Methods in Applied Mechanics and Engineering 332, 644–685.
Wang, J., Poh, L.H., Guo, X., 2023. Localizing gradient damage model based on a decomposition of elastic strain energy density. Engineering Fracture Mechanics 279, 109032.
Westin, C.F., Maier, S.E., Mamata, H., Nabavi, A., Jolesz, F.A., Kikinis, R., 2002. Processing and visualization for diffusion tensor MRI. Medical Image Analysis 6, 93–108.
Winkler, B., Hofstetter, G., Lehar, H., 2004. Application of a constitutive model for concrete to the analysis of a precast segmental tunnel lining. International Journal for Numerical and Analytical Methods in Geomechanics 28, 797–819.
Winkler, B., Hofstetter, G., Niederwanger, G., 2001. Experimental verification of a constitutive model for concrete cracking. Proceedings of the Institution of Mechanical Engineers, Part L: Journal of Materials: Design and Applications 215, 75–86.
Wu, L., Sket, F., Molina-Aldareguia, J., Makradi, A., Adam, L., Doghri, I., Noels, L., 2015. A study of composite laminates failure using an anisotropic gradient-enhanced damage mean-field homogenization model. Composite Structures 126, 246–264.
Yin, B., Zreid, I., Lin, G., Bhashyam, G., Kaliske, M., 2020. An anisotropic damage formulation for composite materials based on a gradient-enhanced approach: Formulation and implementation at small strain. International Journal of Solids and Structures 202, 631–645. doi:10.1016/j.ijsolstr.2020.06.035.
Zreid, I., Kaliske, M., 2014. Regularization of microplane damage models using an implicit gradient enhancement. International Journal of Solids and Structures 51, 3480–3489.

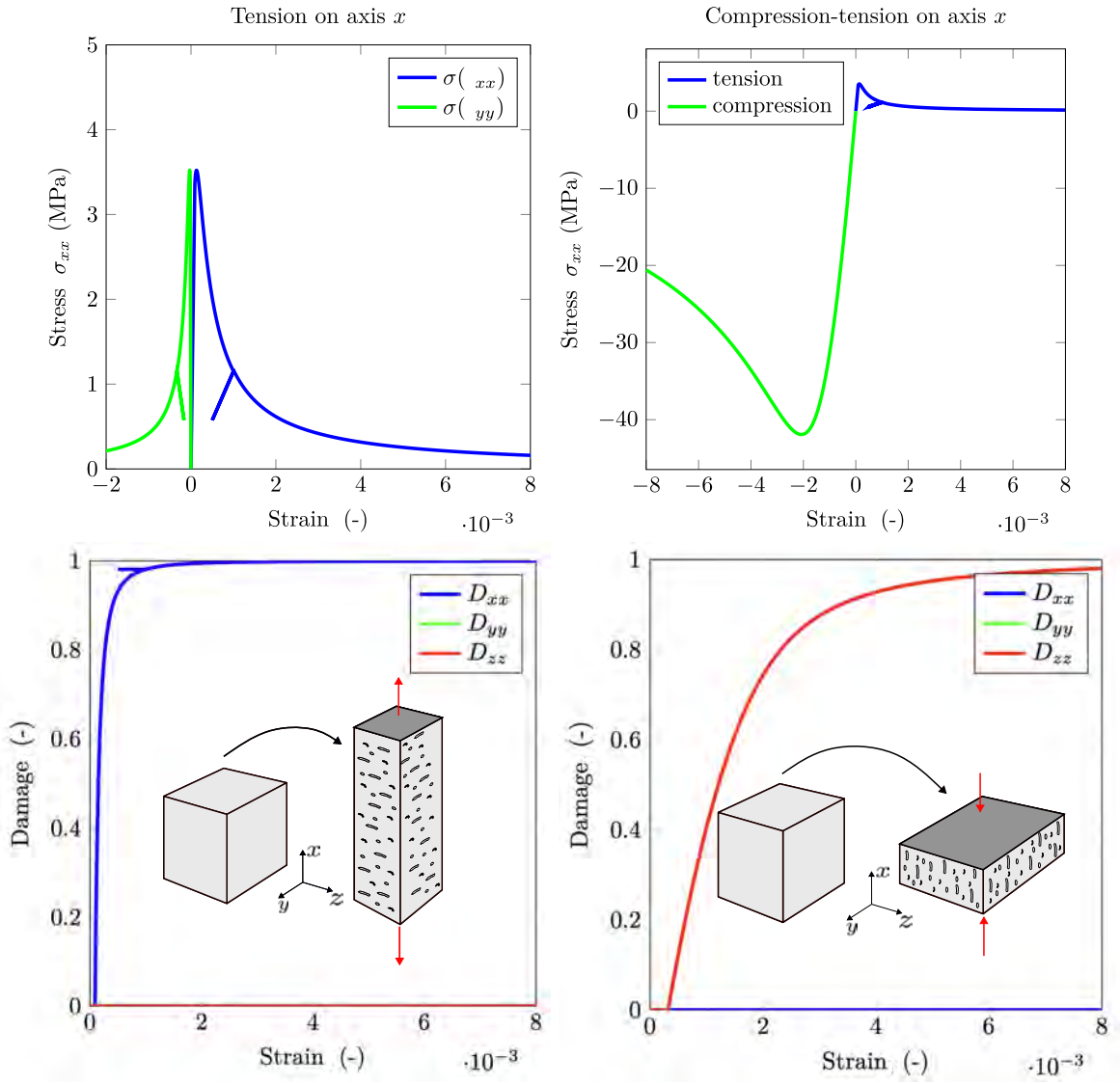

Figure B.20: Desmorat's model response in tension (top-left) and compression (top-right) on axis x. Evolution of damage tensor components under tension (bottom-left) and compression (bottom-right). Micro-cracks are illustraded to highlight the preferential directions of damage.

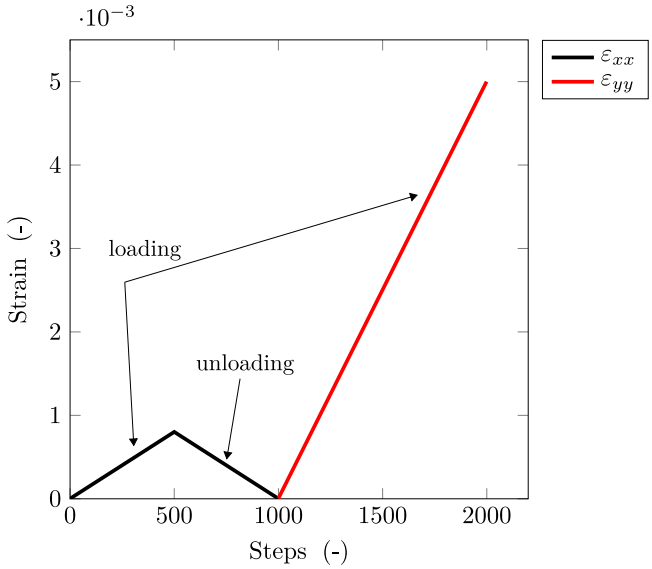

Figure B.21: Non-proportional applied strains at a quadrature point.

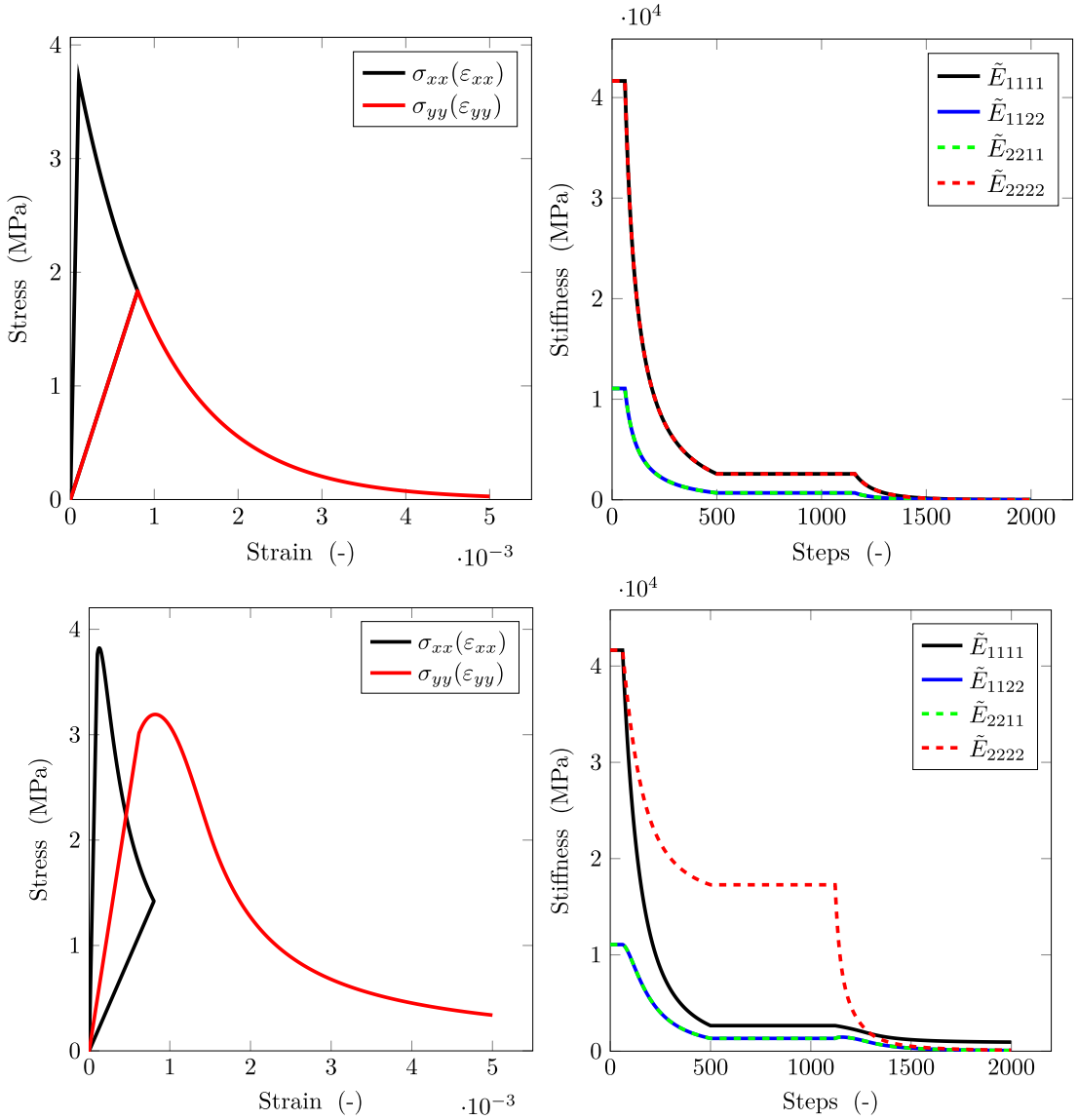

Figure B.22: Isotropic damage model: stress-strain response during non-proportional loading (top-left) and respective evolution of $\mathbb{E}^{\text{iso}}$ components throughout the steps (top-right). Desmorat's model: stress-strain response during non-proportional loading (bottom-left) and respective evolution of $\tilde{\mathbb{E}}$ components throughout the steps (bottom-right).